

5-1-2016

## Ab Initio Structure Determination and Property Characterization of High-Pressure Ca-O Compounds and Li<sub>2</sub>(OH)Br Crystals

Christopher Higgins

University of Nevada, Las Vegas, woodartisans@gmail.com

Follow this and additional works at: <https://digitalscholarship.unlv.edu/thesesdissertations>

 Part of the [Physics Commons](#)

---

### Repository Citation

Higgins, Christopher, "Ab Initio Structure Determination and Property Characterization of High-Pressure Ca-O Compounds and Li<sub>2</sub>(OH)Br Crystals" (2016). *UNLV Theses, Dissertations, Professional Papers, and Capstones*. 2680.

<https://digitalscholarship.unlv.edu/thesesdissertations/2680>

This Thesis is protected by copyright and/or related rights. It has been brought to you by Digital Scholarship@UNLV with permission from the rights-holder(s). You are free to use this Thesis in any way that is permitted by the copyright and related rights legislation that applies to your use. For other uses you need to obtain permission from the rights-holder(s) directly, unless additional rights are indicated by a Creative Commons license in the record and/or on the work itself.

This Thesis has been accepted for inclusion in UNLV Theses, Dissertations, Professional Papers, and Capstones by an authorized administrator of Digital Scholarship@UNLV. For more information, please contact [digitalscholarship@unlv.edu](mailto:digitalscholarship@unlv.edu).

AB INITIO STRUCTURE DETERMINATION AND PROPERTY CHARACTERIZATION  
OF HIGH-PRESSURE Ca-O COMPOUNDS AND  $\text{Li}_2(\text{OH})\text{Br}$  CRYSTALS

By

Christopher A. Higgins

Bachelor of Science – Physics

University of Nevada, Las Vegas

2013

A thesis submitted in partial fulfillment  
of the requirements for the

Master of Science – Physics

Department of Physics and Astronomy

College of Sciences

The Graduate College

University of Nevada, Las Vegas

May 2016

**Thesis Approval**

The Graduate College  
The University of Nevada, Las Vegas

April 12, 2016

This thesis prepared by

Christopher A. Higgins

entitled

Ab Initio Structure Determination And Property Characterization Of High-Pressure Ca-O  
Compounds and Li<sub>2</sub>(OH)Br Crystals

is approved in partial fulfillment of the requirements for the degree of

Master of Science – Physics  
Department of Physics and Astronomy

Changfeng Chen, Ph.D.  
*Examination Committee Chair*

Kathryn Hausbeck Korgan, Ph.D.  
*Graduate College Interim Dean*

Michael Pravica, Ph.D.  
*Examination Committee Member*

Ravhi S. Kumar, Ph.D.  
*Examination Committee Member*

Pamela Burnley, Ph.D.  
*Graduate College Faculty Representative*

# ABSTRACT

## **Ab Initio Structure Determination and Property Characterization of High-Pressure Ca-O Compounds and $\text{Li}_2(\text{OH})\text{Br}$ Crystals**

By

Christopher A. Higgins

Dr. Changfeng Chen, Examination Committee Chair

Professor of Physics

University of Nevada, Las Vegas

Theoretical modeling and computational simulations play an important role in materials research. In this thesis, we report on the study of two material systems using various computational methods. The first material system studied here are  $\text{Ca}_x\text{-O}_y$  compounds under high pressure. Calcium and oxygen are amongst the most abundant elements on Earth, and they form the compound calcium oxide (CaO) that is widely used and very stable at ambient pressures. Although the crystal structure and chemical composition of CaO seems to be simple and well understood, metastable or stable Ca-O compounds with unconventional stoichiometry may exist at high pressures. In this work, first-principles density functional theory calculations and *ab initio* evolutionary simulations have been used to predict high pressure Ca-O structures. We show that under increasing pressure, the stability of the Ca-O system changes and new materials emerge with different stable or metastable structures. In addition to CaO, we systematically examined structures for Ca,  $\text{Ca}_2\text{O}$ ,  $\text{Ca}_2\text{O}_3$ ,  $\text{Ca}_3\text{O}$ ,  $\text{Ca}_3\text{O}_2$ ,  $\text{Ca}_7\text{O}$ ,  $\text{CaO}_2$ ,  $\text{CaO}_3$ ,  $\text{CaO}_7$ , and O at high pressures. The high-pressure phase diagram for these compounds is determined along with the electronic density of states and stoichiometry plots. Our energetic analysis identified three new

stable Ca-O compounds, namely  $\text{Ca}_2\text{O}_3$  and  $\text{CaO}_2$  that are thermodynamically stable above 40 GPa, and  $\text{CaO}_3$  becomes thermodynamically stable at 150 GPa.

The second material system studied in this work is the compound  $\text{Li}_2(\text{OH})\text{Br}$ . This compound has been shown by experiment to be a promising solid electrolyte for advanced solid state ionic battery applications. However, the crystal structure of this compound is highly complex and has not been determined accurately. This has impeded its further investigation and potential applications. We modelled the structure effectively using the density functional theory via VASP software. Having successfully determined the correct structure within our model and confirming it by comparison to experimental XRD results, we then performed other calculations to ascertain the characteristics of this compound. The electronic density of states was determined, along with the phonon density of states and the volume *vs* pressure curve. From the information found within the volume *vs* pressure plot we then determined the bulk modulus of the material.

## ACKNOWLEDGEMENTS

First and foremost I would like to thank Dr. Changfeng Chen for his years of advising and support in my education and research. I feel that through his guidance I have been thoroughly prepared to perform quality research within the scientific community; and I am sure I would not be where I am today without his influence. I would also like to thank Dr. Yi Zhang for his endless patience in helping me to better understand my research. I would also like to acknowledge my research group peers, Andrew Alvarado and William Wolfs. Our hours of discussions and struggles to understand the world of physics have been vital to my education, and I appreciated every minute of it.

# TABLE OF CONTENTS

ABSTRACT.....	iii
ACKNOLWEDGEMENTS.....	v
LIST OF TABLES.....	vii
LIST OF FIGURES.....	viii
CHAPTER 1: INTRODUCTION.....	1
CHAPTER 2: THEORY.....	4
CHAPTER 3: STRUCTURAL MODEL AND METHODS.....	35
CHAPTER 4: RESULTS.....	37
CHAPTER 5: CONCLUSION.....	62
REFERENCES.....	64
CURRICULUM VITAE.....	69

## LIST OF TABLES

Table 1 .....	40
---------------	----



## LIST OF FIGURES

Figure 1 .....	9
Figure 2 .....	10
Figure 3 .....	11
Figure 4 .....	12
Figure 5 .....	13
Figure 6 .....	23
Figure 8 .....	30
Figure 9 .....	31
Figure 10 .....	32
Figure 11 .....	33
Figure 12 .....	38
Figure 13 .....	42
Figure 14 .....	44
Figure 15 .....	45
Figure 16 .....	47
Figure 17 .....	48

Figure 18 .....	49
Figure 19 .....	51
Figure 20 .....	53
Figure 21 .....	56
Figure 22 .....	58
Figure 23 .....	59
Figure 24 .....	61

## LIST OF EQUATIONS

Equation 1.....	17
Equation 2.....	17
Equation 3.....	24
Equation 4.....	59

# CHAPTER 1

## INTRODUCTION

Calcium and oxygen are the fifth and first most abundant elements on Earth, respectively. They form the well-known compound calcium oxide (CaO) that has been proven to be a stable compound with very little in the way of polymorphic attributes having only one stable phase at ambient pressures and a second high pressure phase which results in a body centered cubic (BCC) structure observed through experiments [1]. In chapter 2 of this thesis, crystal structures such as BCC are explained in greater detail. Another reason of particular interest is CaO's simple NaCl structure. The Earth's lower mantle can reach pressures up to 140 GPa, resulting in some very interesting high pressure interactions. Recent studies have shown these new interactions to be a keen insight in understanding how the lower mantle may function. Thus, for the purposes of these calculations we have focused on the simulations that run up to 150 GPa. The specific software used for the computational simulations is explained further in Chapter 2. One would suppose that with CaO's simple structure and how thoroughly it has been studied, and that we would have discovered all there is to know about this particular compound. However with new theoretical techniques showing promising results, we may be learning that we do not know as much as previously thought about simple structures. In fact, in a recent paper [2], it was shown that two new stoichiometry's were found to be thermodynamically stable at high pressures within the compound system of Mg-O. In another well-known compound system of NaCl, using the same theoretical methods, many stable structures were discovered at high pressures, further validating this method and motivating it's use in our simulations [3]. Sodium has only one valence electron, whereas chlorine has 7 valence electrons, however, at high pressures the inner

electrons become available for bonding, which enables the formation of compounds at lower energies. At high pressures, sodium has been observed to possess one other stable phase which leads to the transparency of the element [4]. Calcium has 2 valence electrons which commonly combine in the Earth's mantle with oxygen which has 6 valence electrons. Analyzing such properties as the chemical bonding, and electronic properties, we can begin to understand the particular importance to planetary geology and chemical implications. Calcium has been shown to have multiple high pressure phases in both simulations and experiments; this leads us to believe that this fact will have a profound change on the Ca-O compound system at high pressures [5-14]. With calcium's complex electronic structure, we believe that more high pressure structures will become energetically available for the Ca-O system when it is put under high pressure. Oxygen is also an interesting and well-studied element. It has been observed to have 3 phases below 10 GPa experimentally, and a fourth phase above 96 GPa at which it metallizes [15,16]. With the abundance of oxygen within the Earth's mantle the occurrence of calcium interacting with oxygen should be quite frequent, which adds to the validity of this forming a proper model. In this paper we predict three new thermodynamically stable structures with the compounds  $\text{CaO}_2$ ,  $\text{CaO}_3$ , and  $\text{Ca}_2\text{O}_3$  at high pressures. Within the pressure ranges of 40 GPa, 90 GPa and 150 GPa, certain trends were observed that result in varying the band gap width and led to structures changing between insulating and semi-conducting properties of the structures. We performed extensive first principal calculations combined with an automated structure search method. Using the new evolutionary algorithm Universal Structure Predictor: Evolutionary Xtallography (USPEX) for our structure search method, we have fully constructed a phase diagram from 0 GPa to 225 GPa for the Ca-O system. We determined that three compounds are stable at higher pressures by calculating their formation energies. We used a first

principles method using the augmented plane wave method (PAW) [17], which makes no approximations other than the local density approximation (LDA) [18]. This allows us to calculate such properties as the electronic structures, phase transitions and equations of state.

In this thesis, we also present the results of our  $\text{Li}_2(\text{OH})\text{Br}$  study. This particular compound has been under investigation experimentally and has been shown to have possible properties particularly desirable for advanced battery applications. The compound was successfully modeled in accordance with an accompanying x-ray diffraction (XRD) pattern that was acquired experimentally. The density of states was also calculated and showed promising results when compared with another well studied compound  $\text{Li}_3\text{OBr}$ . A pressure vs. volume curve was created and accompanied with a bulk modulus that agreed well with the known compound of  $\text{Li}_3\text{OBr}$ . Finally, a phonon partial density of states plot was created which can be a benefit in revealing more information about this particular compound in the future.

# CHAPTER 2

## Theory

In order to begin understanding quantitative ab-initio calculations and solid state properties, we must first begin by understanding the many body Schrödinger equation. If we first examine the Hamiltonian, (which contains the kinetic energy of all the particles) in a particular problem we can start to peruse a material of choice and examine how energies interact with each other. The next important step is to evaluate the two types of electrons: core electrons and valence electrons. In chemical bonding, valence electrons contribute to chemical bonds; whereas core electrons strongly bind themselves within the closed shells of lattice ions. This in turn has a smaller contribution in terms of solid state properties. If we continue to follow this line of thinking, we can study a particular material and view it as a compound with two individual components, the lattice ions and the valence electrons. This of course can only be a first approximation. We will begin by establishing some units, where  $\left(\frac{e^2}{4\pi\epsilon_0} = m_e = \hbar = 1\right)$ .

The Hamiltonian for this type of system will look like the following:

$$H = H_{el} + H_{ion} + H_{el,ion} + H_{ext}$$

Within this equation exists the entire kinetic energy of the valence electrons and the ions, as well as the interaction between these particles and any probably interactions that exist within external fields. The external field portion is something that can obviously be left out in certain cases where no such field exists. We can then begin by examining the other terms.

For the electron portion:

$$H_{el} = H_{el}^{kin} + H_{el,el} = \sum_k \frac{p_k^2}{2} + \frac{1}{2} \sum_{kk', k \neq k'} \frac{1}{|r_k - r_{k'}|}$$

We can see that this equation consists of the Coulomb interaction between all the electrons and their kinetic energies. The summations include all indices except for when k equals itself. We also include the momentum  $\vec{p}_k$  and the position  $\vec{r}_k$  for all possible k electrons.

For the ionic portion:

$$H_{el} = \sum_{k,i} V_{el,ion}(r_k - R_i)$$

For this portion, we construct the equation based on the ion-ion interaction. This interaction is the sum of a two particle interaction between both ions and electrons and is dependent only on this distance to one another.

These equations complete the picture we are trying to construct when trying to understand quantum mechanically the aspects of materials. We must now transition from the Hamiltonian function to the Hamiltonian operator. We can use the electron and ionic coordinates in conjunction with the coordinate representation of the Hamiltonian operator to determine the wave function which is a function of all of the corresponding coordinates. Within the Hamiltonian are parts that we can solve very precisely for, however there are other parts in which we must make approximations. One such approximation involves partially ignoring or even completely ignoring certain parts of the equation, and then making up for their removal by using lattice symmetry to further reduce the simplification. When we ignore individual interactions between the terms of the Hamiltonian we create problems because of the Coulomb



interactions. In order to have a valid approximation, we must at least compensate for the negative electron charge.

We begin by looking at a first approximation. The jellium or uniform electron gas model is ideal because it includes the average charge of the ions and does so by defining a uniform space charge  $p_+$  which the electrons interact with it. We will represent this in our equation by  $H_+$  and this can be seen as:

$$H_{el} = \sum_k \frac{\nabla_k^2}{2} + \frac{1}{2} \sum_{kk', k \neq k'} \frac{1}{|r_k - r_{k'}|} + H_+$$

By doing this, lattice symmetry no longer plays a role and we can see the electron-electron interaction. By defining which ions are fixed at their equilibrium positions in conjunction with the constant space charge, we can also define the ionic lattice which allows us to further refine our equation. By making this adjustment, our Hamiltonian becomes more complicated, which requires us to make further approximations. If we use the same methodology in order to represent the ions, we can view them as moving in a negative space charge  $p_-$ . Once again applying this to our equation:

$$H_{ion} = - \sum_i \frac{\nabla_i^2}{2} + \frac{1}{2} \sum_{ii', i \neq i'} V_{ion}(R_i - R_{i'}) + H_-$$

We can now split up our second term into an equilibrium part, and a phonon part. This enables a starting point for studying lattice dynamics. Thus far we have delineated our problem into two portions. In the first portion, we consider the electrons movement in a stationary lattice; for the second portion, we consider the movement of ions among a uniformly spaced charge of electrons. What we have just set up is called the adiabatic approximation; this essentially is too

determine whether or not the faster electrons will respond adiabatically to a change in positions in conjunction with the heavy ions. Comparatively, the ions will only make changes in positions very slowly within the electron system. If we are interested in seeing the electronic motion we need to look at the instantaneous positions of the ions. This will now let us alter the Schrödinger equation so that it looks like:

$$(H_{el} + H_{el-ion})\psi = E_{el}\psi$$

$$\psi(r_1\sigma_1 \dots r_N\sigma_N; R_1 \dots R_{N'})$$

This represents our many body wave equation with fixed ionic positions which is a function of all electron positions and spins. The ionic positions are then set within the parameters.

## CRYSTAL STRUCTURES

A good way to differentiate materials is by looking at their crystal structures. One of the main ideas in crystallography is to find a structure represented by an elementary unit cell and then to repeat it infinitely in all directions until it represents the material a person would be trying to model. Fundamentally, the Bravais lattice can describe how this elementary unit cell can be arranged periodically to represent a real material. Within this unit cell, various building blocks can be used, such as molecules, atoms, ions or other particles. In order to be a Bravais lattice, it must consist of an infinite array of discrete points, and this infinite array must see exactly the same within its orientation and arrangement no matter what point the viewer is observing from. If we project a three-dimensional Bravais lattice, we can represent it with a position vector  $R$  in the form of:

$$R = n_1 a_1 + n_2 a_2 + n_3 a_3$$

In the equation,  $n_i$  represents the integers, while  $a_i$  represents the primitive vectors. The primitive vectors are the fundamental vectors that make up the primitive cell, which in turn represents the minimum volume the correct cell will have. The number of atoms that constitute a primitive cell are always the same, however, there are many possible primitive cells within a lattice. Taking a lattice point, and then adding an identical basis of atoms to every lattice point, this would form a crystal structure.

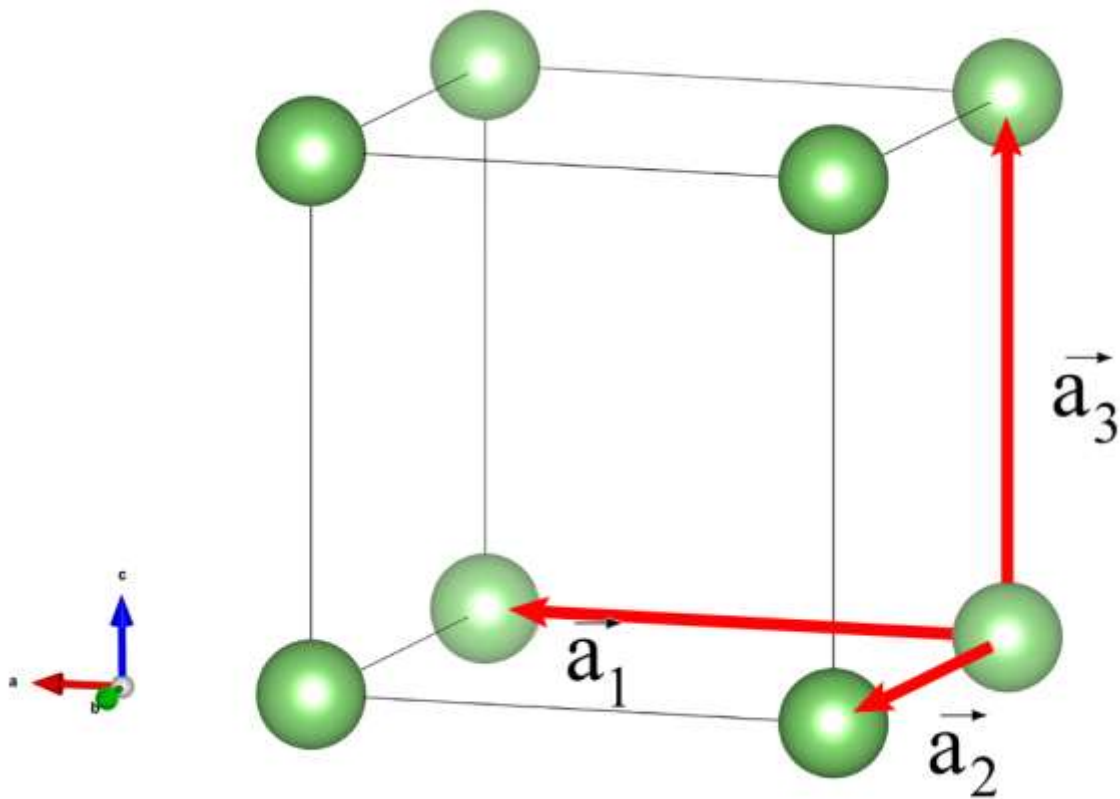


**Figure 1: A simple cubic structure represented by a unit cell**

In a three dimensional Bravais lattice, the simple cubic (sc) lattice is the most well known because of its basic cubic shape. This lattice is generated by three primitive vectors which are all perpendicular to one another, but of equal length as indicated by the red lines in figure 1. An elemental example of this structure would be polonium.

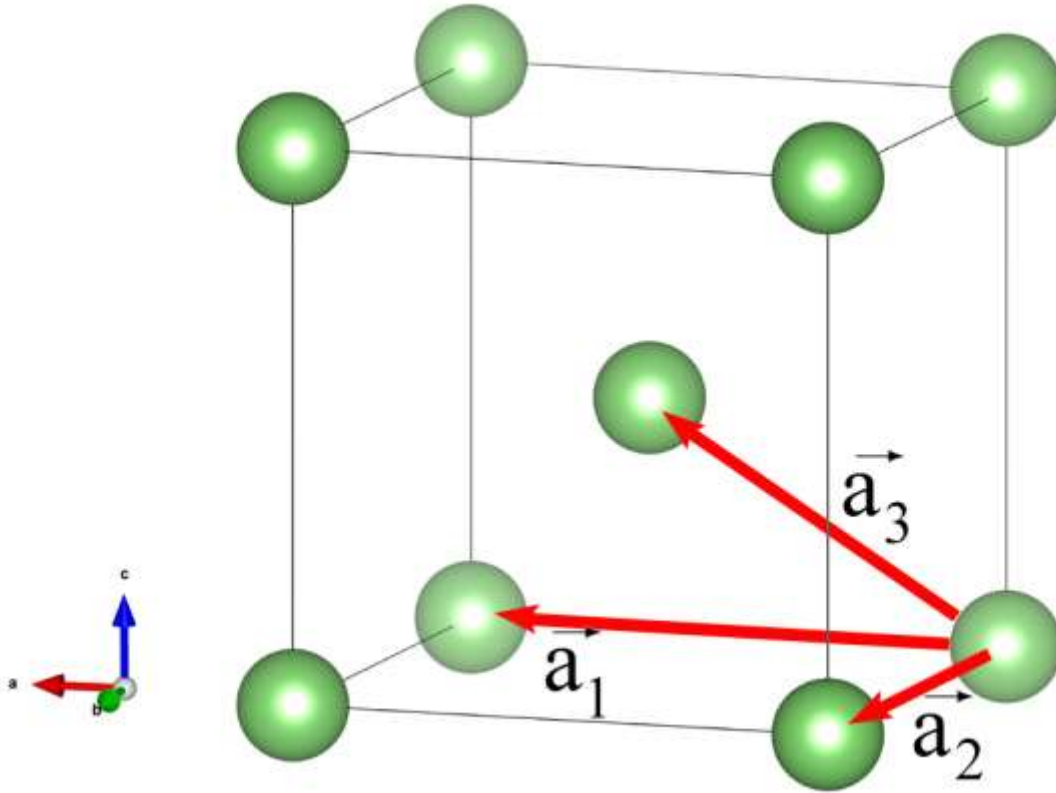


Figure 2: A unit cell of a body centered cubic lattice.

Another very commonly observed example is the body-centered cubic (bcc) Bravais lattice. We can see how this lattice is constructed in terms of primitive vectors by the following:

$$a_1 = a\hat{x}, a_2 = a\hat{y}, a_3 = \frac{a}{2}(\hat{x} + \hat{y} + \hat{z})$$

We can rewrite a more symmetric version:

$$a_1 = \frac{a}{2}(\hat{y} + \hat{z} - \hat{x}), a_2 = \frac{a}{2}(\hat{z} + \hat{x} - \hat{y}), a_3 = \frac{a}{2}(\hat{x} + \hat{y} - \hat{z})$$

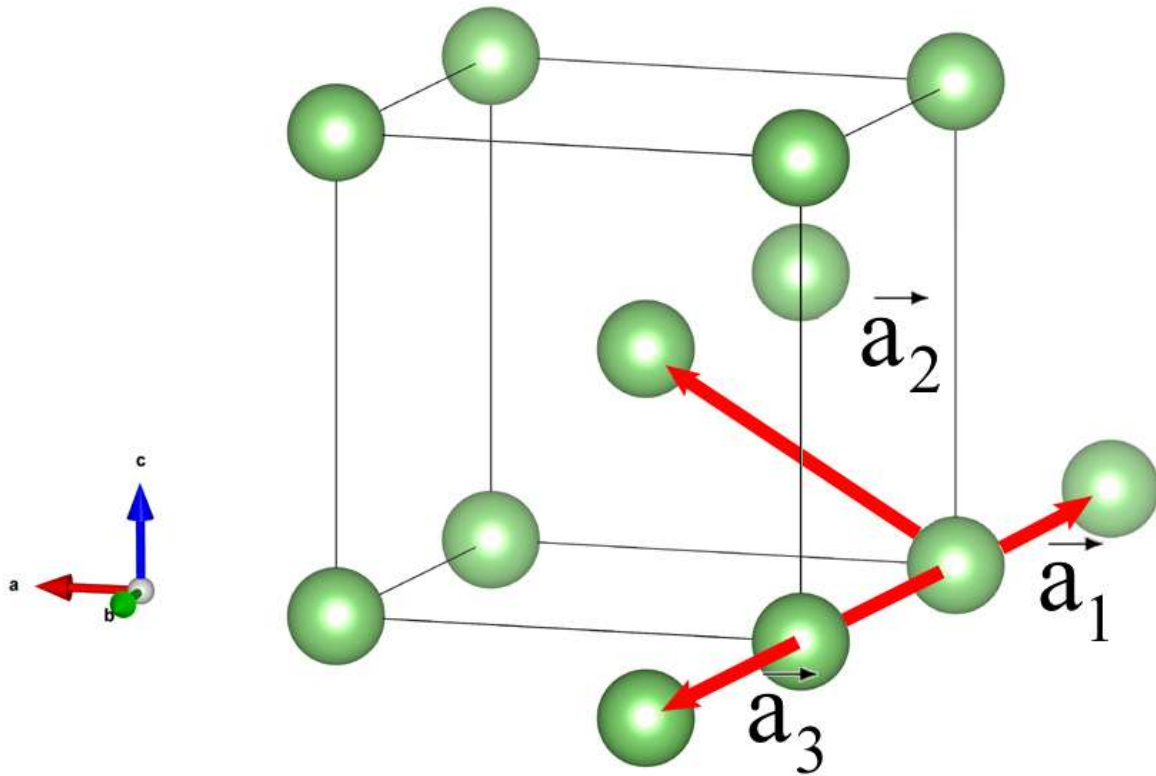


**Figure 3: A body centered cubic crystal lattice. Lattice points are extended beyond a single unit cell to show how additional unit cells are included.**

A bcc crystal lattice has been constructed as an example in Figure 2 and it is evident how the third lattice vector has led to an atom position at the center of the lattice. To continue the crystal lattice in order get a more complete picture of how the lattice becomes a larger material, we can look at Figure 3 to ascertain how the atoms extend to form adjacent unit cells. This is a very common crystal structure in metals with some examples of lithium and iron.

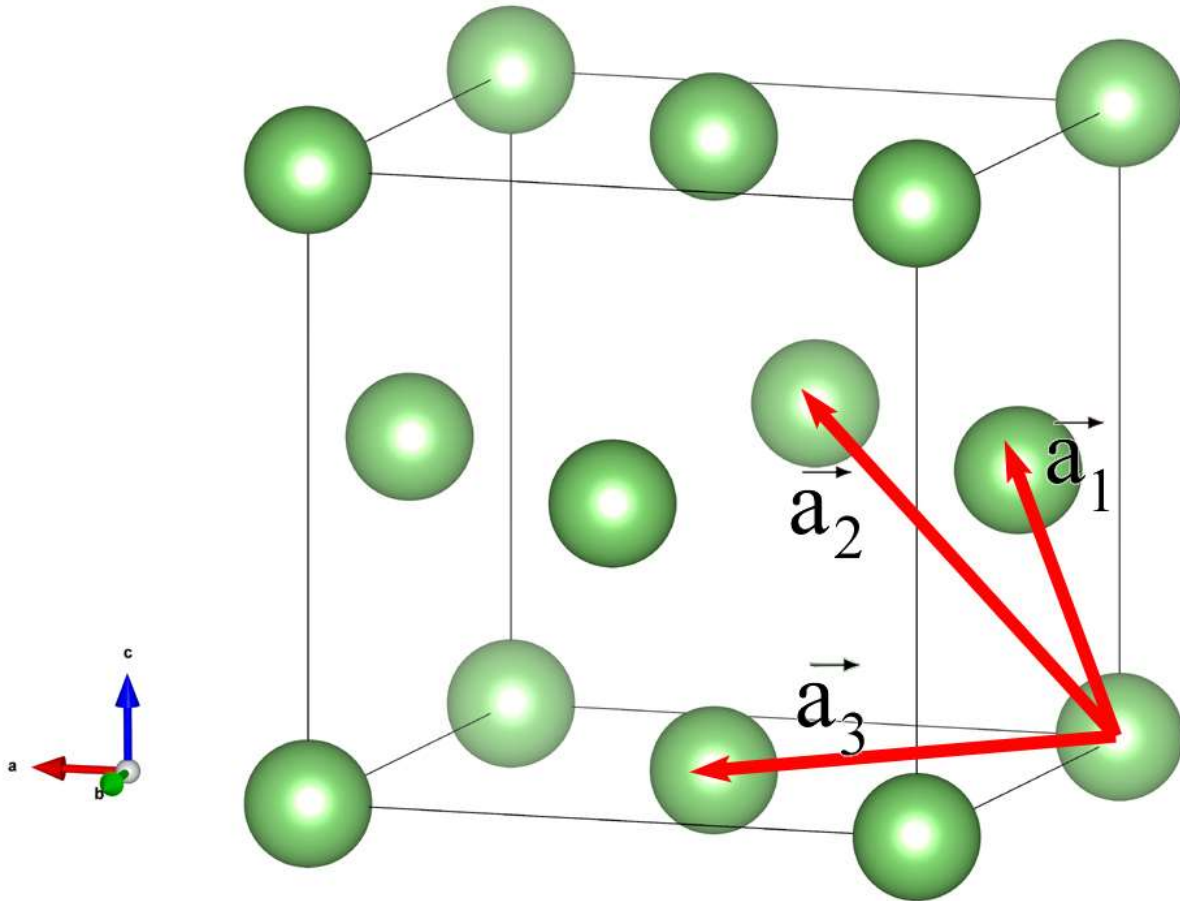


Figure 4: A unit cell of a face centered cubic structure.

One of the primary compounds studied in this work is calcium oxide. The structure of this compound is fairly well-known and is our next example, face centered cubic (fcc) Bravais lattice. It can be constructed by taking a simple cubic lattice and adding an atom at the center of all the faces. We can see a symmetric set of primitive vectors is comprised of:

$$a_1 = \frac{a}{2}(\hat{y} + \hat{z}), a_2 = \frac{a}{2}(\hat{z} + \hat{x}), a_3 = \frac{a}{2}(\hat{x} + \hat{y})$$

## LATTICE PLANES

If we look at a Bravais lattice from three different atomic positions that are non-collinear, we can define a lattice plane. We can then see that every lattice plane consists of infinitely many lattice points which are in translational symmetry.

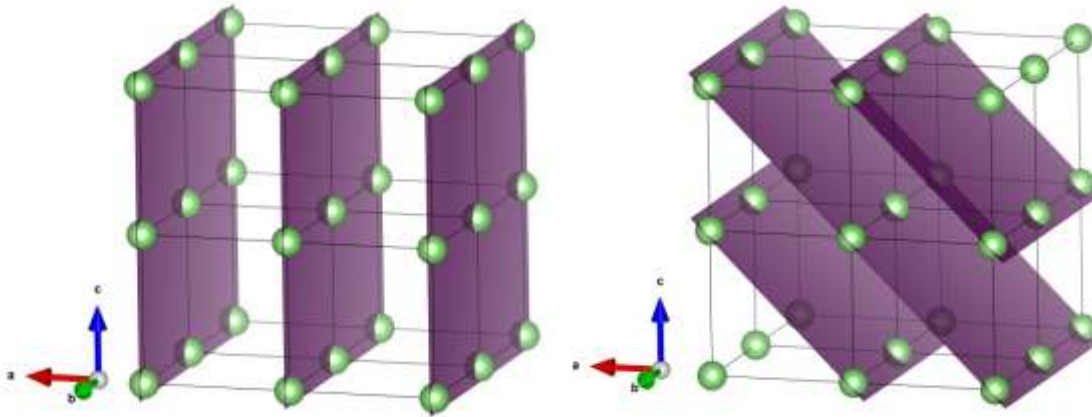


**Figure 5: Lattice planes showing on a simple cubic structure.**

Now we can discuss a family of lattice planes which is a set of parallel and equally spaced planes that contain all of the Bravais points of the three dimensional lattice.



## MILLER INDICES

To classify all possible lattice plane families, we simply need to look at the reciprocal lattice. The theorem of interest says that for any family of lattice planes, there is a reciprocal lattice vector perpendicular to those planes and separated by a distance  $d$ . The shortest length can be found from  $\frac{2\pi}{d}$ . From this we can also see that if we have a reciprocal lattice vector  $K$ , then there is a family of lattice planes a distance  $d$  away that is perpendicular. Once again, the way to find the shortest reciprocal lattice vector which is parallel to  $K$  is by the formula  $\frac{2\pi}{d}$ . These coordinates that are based on the shortest vector parallel to  $K$  are known as the Miller indices.

A plane that has the Miller indices  $h,k,l$  can be said to be perpendicular to the reciprocal lattice vector  $hb_1 + kb_2 + lb_3$ . In order to identify a certain lattice plane, the Miller indices can be used for this purpose. In our case of calcium oxide we begin with the low index surfaces (100), (110) and (111) of the fcc Bravais lattice. The indices describe the vectors that are within the direct lattice. We can define a vector by using the  $[hkl]$  system:  $ha_1 + ka_2 + la_3$ . In order to make this vector perpendicular to the  $(hkl)$  plane it needs to be in a cubic lattice. So we have created an instance where the lattice and the reciprocal vectors are orthogonal and the  $(hkl)$  and  $[hkl]$  are both denoting normal planes that are within normal directions in Cartesian coordinates. If we look at the simpler primitive lattice vectors for fcc and bcc we can see that they are not orthogonal. The Miller indices for these specific lattices can be defined relative to the lattice vectors of a cubic supercell, which will once again lead us to Cartesian directions.

## DENSITY FUNCTIONAL THEORY

When we examine at the modeling of a particular material, we begin with its most elementary constituents. One important particle that we study very closely is the electron; which largely interacts via the electrostatic Coulomb interaction. Frequently the goal is to describe the electrons quantum mechanically, but in some cases it is more beneficial to treat them classically. For the circumstances we are investigating, we examined the valence electrons for the atomic elements in question. Because the elements in question are of a lighter nature and moving much slower than the speed of light, this justifies treating the valence electrons using the non-relativistic Schrödinger equation. This simplification solves some possible issues, but there is still the problem that the many body Schrödinger equation cannot be solved for a system with approximately  $10^{23}$  electrons. This is where density functional theory (DFT) provides a solution to this problem. DFT effectively handles this problem by computing the total electron density of the system.

## KOHN-SHAM THEOREMS

As stated previously, there are a few approximations when modeling elements and compounds computationally, DFT is based around two mathematical theorems that were produced by Hohenberg and Kohn [19], and then of course the set of equations that were produced by Kohn and Sham[20]. The first theorem states: “The ground-state energy of a system of interacting electrons as described by the Schrödinger equation is a unique functional of the total electron density.” [21] From this statement, it is evident that there is actually a one-to-one mapping between the ground state electron density and the many body ground state wave-function. One of the other benefits that this theorem provides is the fact that it determines uniquely all of the properties in the ground state, such as the wave-function and energy. The problem with this theorem is that it only shows the existence of the functional and not what it actually represents. In order to get more information about it we need to use the second theorem, the Hohenberg-Kohn theorem, which states: “The electron density that minimizes the energy of the overall functional is the true electron density corresponding to the full solution of the Schrödinger equation.” [22] If we can minimize this functional effectively, that should give us its true value and in turn show us the corresponding electron density. This is in fact the variational principle that is used in practice within computational theory groups that uses approximated forms of the functional. A summary of the Kohn-Sham spin-density functional method has been published before [23], which is the most widely used in modern computational simulations. It also addresses a common need to calculate the ground-state energy  $E$  along with the spin densities  $n_{\uparrow}(r), n_{\downarrow}(r)$  for a system of  $N$  electrons that are exposed to some external potential  $v(r)$  which is very frequently caused by the nuclei. We can do this by solving the one-electron equations which are also known as the Kohn-Sham equations.

The Kohn-Sham equations look like the following:

$$\left(-\frac{1}{2}\nabla^2 + v(r) + u([n]; r) + v_{XC}^\sigma([n_\uparrow, n_\downarrow]; r)\right)\psi_{\alpha\sigma}(r) = \epsilon_{\alpha\sigma}(r) \quad (1)$$

and

$$n_\sigma(r) = \sum_{\alpha} \Theta(\mu - \epsilon_{\alpha\sigma}) |\psi_{\alpha\sigma}(r)|^2, n(r) = n_\uparrow(r) + n_\downarrow(r)$$

In the equation  $\sigma$  represents the z component of the spin and  $\alpha$  represents the remaining quantum numbers.  $\Theta(\mu - \epsilon_{\alpha\sigma})$  Represents a Heaviside function and it ensures that all of the occupied spin orbitals are occupied by a single electron and that all of the other orbitals remain empty when  $\epsilon_{\alpha\sigma} > \mu$ . Then we consider at the chemical potential:

$$\int d^3r n(r) = N$$

Additionally, we can peruse the external potential portion represented by  $v(r)$  and then evaluate equation (1) to determine the effective potential and how it contains the classical Hartree potential:

$$u([n]; r) = \int d^3r' \frac{n(r')}{|r - r'|}$$

In addition, there is also a spin dependent exchange-correlation potential  $v_{XC}^\sigma([n_\uparrow, n_\downarrow]; r)$  which is a functional of the spin densities. If considering the two Kohn-Sham equations, it is evident that they are intertwined within the spin density  $n_\sigma(r)$ . Because of this it can also be seen that this is only solvable via self-consistent iteration. We will now investigate at the total electron energy which is given by:

$$E = T_s[n_\uparrow, n_\downarrow] + \int d^3r n(r)v(r) + U[n] + E_{XC}[n_\uparrow, n_\downarrow] \quad (2)$$

And with,

$$T_s[n_\uparrow, n_\downarrow] = \sum_{\sigma\alpha} \Theta(\mu - \epsilon_{\alpha\sigma}) \langle \psi_{\alpha\sigma} | -\frac{1}{2} \nabla^2 | \psi_{\alpha\sigma} \rangle$$

And so we use the notation:

$$\langle \psi_{\alpha\sigma} | \hat{O} | \psi_{\alpha\sigma} \rangle = \int d^3r \psi_{\alpha\sigma}^*(r) \hat{O} \psi_{\alpha\sigma}(r)$$

Here,  $T_s$  is the non-interacting kinetic energy, which it can also be seen that it is a functional of spin densities. This is because the external potential  $v(r)$  is a functional of spin densities, this leads us to the conclusion that the Kohn-Sham orbitals are also spin density functionals. We note that the second term in equation (2) is the electron nuclei interaction. The third term,  $U[n]$ , is the electrostatic Hartree term and includes the self-repulsion of the electron density.

$$U[n] = \frac{1}{2} \int d^3r d^3r' \frac{n(r)n(r')}{|r - r'|}$$

For the final term we consider the exchange correlation energy,  $E_{XC}$ , where the derivative of this energy is taken, we will obtain the exchange correlation potential.

$$v_{XC}^\sigma([n_\uparrow n_\downarrow]; r) = \frac{\delta E_{XC}}{\delta n_\sigma(r)}$$

If we sought to obtain the total energy, then, using equation (2) which is a beginning in the description of the total electronic energy. But in order to complete the picture, we must include the electrostatic repulsion of the atomic nuclei, which, by the definition is included in the term  $E_{XC}$ . For everyday computational use, the term  $E_{XC}[n_\uparrow n_\downarrow]$  must be approximated.

## LDA

One approximation that has been both valuable and popular uses the local density to define the exchange correlation functional and is named after how it functions, local density approximation (LDA). The LDA method can be defined by:

$$E_{XC}^{LDA}[n(r)] = \int d^3r n(r) e_{XC}^{unif}(n(r))$$

$e_{XC}^{unif} = e_X^{unif} + e_C^{unif}$  has been derived as a known exchange correlation energy per particle based on a gas of uniform electron density. It can be divided into correlation and exchange components  $e_C^{unif}$  and  $e_X^{unif}$  [24,25]. Within the homogenous electron gas, the solution is known for the exchange energy density  $e_X^{unif}$ , with that piece solved we can use LDA to approximate the exchange energy of a system that has a non-homogenous density by using the homogenous solution, point-by-point, in a system which results in:

$$E_X^{LDA}[n(r)] \propto \int d^3r n(r)^{\frac{4}{3}}$$

As has been observed in experimental studies, the correlation energy density  $e_C^{unif}$  has an analytical solution of the homogenous system, but is only valid for the low and high density limits [26]. However, it has been recently shown that Monte Carlo simulations have successfully obtained accurate values in the intermediate density range [27]. In today's use of the LDA method, it is common to extract the key components that came from these simulations and reproduce similar results in other applications.

## GGA

Another very popular functional is the generalized gradient approximation (GGA). GGA, like LDA, is still a local approximation, but it takes into account the gradient of the density at the same position. It has been shown that the use of the GGA functional provides very good results for ground state energies and molecular geometries [28-31]. There are some differences between LDA and GGA that make one method more favorable than the other in certain situations. GGA is considered to be good at improving total energies, atomization energies, energetic barriers, and structural differences when compared to other exchange correlation functionals [32]. On the other hand, GGA is known to expand and soften bonds, which has an effect of over correction. It has also been noted that a semi-empirical GGA can be very accurate for small molecules, but fails when trying to approximate a delocalized set of electrons in a uniform gas, and this failure transfers to simple metals. Within this thesis we studied the element oxygen in its solid form and within this form at low pressures that include the alpha and delta phases, oxygen possesses a magnetic moment. This magnetic moment is very unusual and can be problematic when trying to model such a structure. The LDA method does not deal with this magnet moment very well and GGA would be better suited to handle it. However, our area of interest in dealing with CaO lies at higher pressures which includes other solid oxygen phases, the epsilon phase and the zeta phase. It has been seen that the magnet moment is destroyed upon the phase transition between the delta phase and the epsilon phase at approximately 10 GPa. Because the magnetic moment is destroyed, LDA becomes a better choice when choosing exchange correlation functionals. Thus LDA has been used in this thesis to explore all high pressure phases

## VASP

The Vienna Ab initio Simulation Package (VASP) is a software program that utilizes DFT, and is used for ab-initio quantum-mechanical molecular dynamics simulations. It accomplishes this task by using pseudopotentials or the projector-augmented wave (PAW) method involves a plane wave basis set [33-35]. This is accomplished by using the finite temperature LDA functional with the free energy as the variational quantity. Using molecular dynamics, the instantaneous electronic ground state is assessed at each calculated step within the molecular dynamic simulation. In the original Car-Parinello method, a simultaneous integration of the equations of motion for the ions and electrons are described. This technique however, had its own inherent problems that had to be overcome. The issue was handled by the efficient use of matrix diagonalization and also the use of efficient Pulay/Broyden mixing to accurately calculate the charge density used by VASP. The interactions can be described from this by the use of ultra-soft Vanderbilt pseudopotentials (US-PP) or within the PAW method [36,37]. For transition metals and first row elements, both of these approaches are good at reducing the number of plane waves per atom by a significant amount. Some of the goals that VASP can achieve are quite useful; chief amongst them is to allow one to calculate the forces and the full stress tensor which in the end can be used for the relaxation of atoms into their instantaneous ground states.



## ALGORITHMS USED IN VASP

VASP essentially uses two loops within its program. First, there is an outer loop, this loop optimizes the charge density and the second loop works on optimizing the wavefunctions. The algorithms that VASP uses are described as an iterative matrix-diagonalization scheme. These algorithms are actually based on the conjugate gradient scheme [38,39], the residual minimization scheme-direct inversion of the iterative subspace (RMM-DIIS) [40,41] or the Block Davidson scheme [42,43]. In order to get an efficient charge density mix, the Broyden/Pulay mixing scheme must also be efficient [44-46]. In Figure 6 a flow chart of how VASP uses its algorithms is displayed. It can be seen that within the Hamiltonian there are several self-consistency loops that are related by the charge density and the wavefunction, and they are optimized iteratively so that they can get closer and closer to the exact wavefunction of a particular Hamiltonian. From these loops an optimized wavefunction is created and from this it is then used to calculate a new charge density. This density is then mixed with the old charge density in order to evolve correctly.

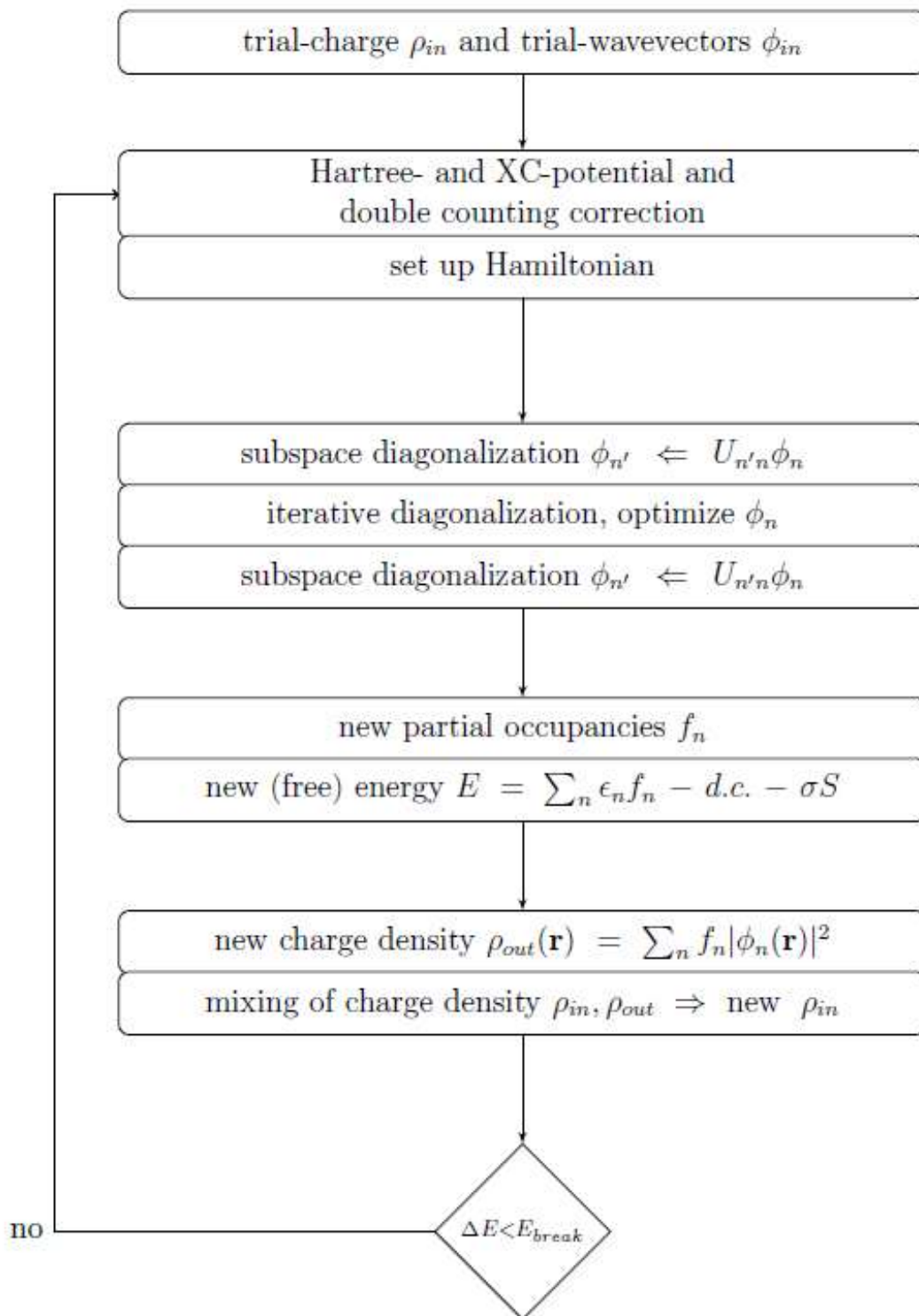


Figure 6: Flow chart of how VASP works. Shown is a calculation of the KS-ground-state

## PROJECTOR AUGMENTED WAVE (PAW)

The projector augmented wave (PAW) method is a solution to the problem of having rapid oscillations of the wavefunction located at the core region because of high kinetic energy of the electrons and in turn the reverse situation where the bonding region requires a large complete basis set for the smoother parts of the wave function [47]. To counteract this problem, the use of the pseudopotential method and augmented wave method are best suited. This is where the PAW method becomes helpful as it extends these methods and combines them in order to create a unified electron structure method.

The foundation of the PAW method lies in what is known as transformation theory which is essentially where one maps a true wavefunction  $|\psi_n\rangle$  is mapped onto an auxiliary wavefunction  $|\tilde{\psi}_n\rangle$  while still retaining the complete nodal structure of the true wavefunction. The index  $n$  is what labels the one particle states along with a band index, k-point and spin index. The goal of this method is to obtain smooth auxiliary wavefunctions which will be expanded into plane waves with fast convergence. We can denote  $T$  to represent the transformation from the auxiliary wavefunctions to the physical wavefunctions.

$$|\psi_n\rangle = T|\tilde{\psi}_n\rangle \quad (3)$$

Equation 3 is defined as our transformation operator and can be described in the following fashion; the goal is to get to the correct nodal structure with the resulting wavefunctions  $T$  which has to change the auxiliary wavefunctions in each atomic region. We can then define:

$$T = 1 + \sum_R S_R$$

This is the sum over atomic sites  $R$  and accounts for the differences between the wavefunctions.  $S_R$  Represents the operators, which are local terms and defined as solutions  $|\phi_i\rangle$  for the isolated

atoms. These partial waves represented by  $|\phi_i\rangle$  are used as a basis set to express the corresponding valence wavefunctions.

$$\psi(r) = \sum_{i \in R} \phi_i(r) c_i \text{ for } |r - R_R| < r_{c,R}$$

$c_i$  represents the coefficients that are still unknown. For the other notations, the index  $i$  covers the site index  $R$ , and then the angular momentum indices  $(l, m)$  along with a partial wave index for differentiation the partial waves with the aforementioned quantum numbers  $(l, m)$  at the same site  $R$ . The partial waves are not always bound states, for this reason they are not normalizable. Because of this, they need to be truncated at a central radius  $r_{c,R}$ . The way the PAW method has been designed is to make sure that the final results are also independent of the cutoff location unless the user chooses it to be close to the nucleus. The core wavefunctions are contained within the core regions and do not spread out to their neighboring atoms, so they will be treated differently. In this instance, we are using the frozen-core-approximation, thus, the energies and densities of the core electrons are identical to those of the isolated atoms.  $T_R$  must produce wavefunctions that are orthogonal in order to be useable to the core states. When we treat the core states separately, they will be treated differently. Now, for every partial wave, we must pick an auxiliary wave  $|\phi_i\rangle$ . We examine at the following equations:

$$|\phi_i\rangle = (1 + S_R)|\tilde{\phi}_i\rangle \text{ for } i \in R$$

$$S_R|\tilde{\phi}_i\rangle = |\phi_i\rangle - |\tilde{\phi}_i\rangle$$

These equations define the local contribution,  $S_R$ . We state that  $1 + S_R$  will change so that the wavefunction will only change locally and it is required that the partial waves  $|\phi_i\rangle$  and the corresponding auxiliary waves  $|\tilde{\phi}_i\rangle$  will match each per pair of corresponding points beyond the cutoff radius  $r_c$ :

$$\phi_i(r) = \tilde{\phi}_i(r) \text{ for } i \in R \text{ and } |r - R_R| < r_{c,R}$$

From this, it is evident that there is only one way that we can use this transformation vector with any auxiliary wavefunction, we must expand the auxiliary wavefunctions locally into the auxiliary partial waves.

$$\tilde{\psi}(r) = \sum_{i \in R} \tilde{\phi}_i(r) \langle \tilde{p}_i | \tilde{\psi} \rangle \text{ for } |r - R_R| < r_{c,R}$$

The projector functions  $|\tilde{p}_i\rangle$  can be defined as the probe of the local character of the auxiliary wavefunction in the atomic region. If we look closer at  $r_c$  we have  $\sum_i |\tilde{\phi}_i\rangle \langle \tilde{p}_i| = 1$ . It is also apparent via insertion that the equation holds for any auxiliary wavefunction if:

$$\langle \tilde{p}_i | \tilde{\phi}_j \rangle = \delta_{ij} \text{ for } i, j \in R$$

We must also note that the projector functions and the partial waves do not need to be orthogonal. Now we can combine these equations and apply  $S_R$  for any auxiliary wavefunction:

$$S_R |\tilde{\psi}\rangle = \sum_{i \in R} S_R (|\tilde{\phi}_i\rangle \langle \tilde{p}_i | \tilde{\psi} \rangle) = \sum_{i \in R} (|\phi_i\rangle - |\tilde{\phi}_i\rangle) \langle \tilde{p}_i | \tilde{\psi} \rangle$$

This then leads us to the transformation operator:

$$T = 1 + \sum_i (|\phi_i\rangle - |\tilde{\phi}_i\rangle) \langle \tilde{p}_i |$$

Examining the  $i$  index, we note that it covers all partial waves of atoms. If we use the definition of the projection operator  $\hat{T}$ .

$$|\psi\rangle = |\tilde{\psi}\rangle + \sum_i (|\phi_i\rangle - |\tilde{\phi}_i\rangle) \langle \tilde{p}_i | \tilde{\psi} \rangle = |\tilde{\psi}_n\rangle + \sum_R (|\psi_R^1\rangle - |\tilde{\psi}_R^1\rangle)$$

Then we have two one-center expansions...

$$|\psi_R^1\rangle = \sum_{i \in R} |\phi_i\rangle \langle \tilde{p}_i | \tilde{\psi} \rangle$$

$$|\tilde{\psi}_R^1\rangle = \sum_{i \in R} |\tilde{\phi}_i\rangle \langle \tilde{p}_i | \tilde{\psi} \rangle$$

We need to decide at this point if this auxiliary function provides the true wavefunction. We can think of the transformation as a change of representation, somewhat like a coordinate transformation. In order to get the correct wavefunction, the transformation of the total energy functional must be calculated consistently which will result in a minimum and ensure the correct wavefunction as a result. If we look at the different regions in space we can better understand the equation being used and its influence over the true wavefunction. It is evident that when the atoms are very far from the partial waves, the auxiliary wavefunction is then equal to the true wavefunction  $\psi(r) = \tilde{\psi}(r)$ . If we look at the opposite case when the atoms are very close we see  $\psi(r) = \psi_R^1(r)$ . For this case, the wavefunction will be constructed from the partial waves that have the correct nodal structure. For use in simulations, we must truncate this infinite set of waves in order to complete the calculation, this means that equation 4 isn't used exactly as it is shown. In turn this means that the atomic region of the plane wave will contribute to the true wavefunction. The reason for doing this is that it allows for fast convergence of the partial wave expansion which is because of the missing pieces, but these are compensated for because of the plane waves.

## K-POINTS

One of the important parameters in DFT calculations is calculating the averages for the states that are within the Fermi surface which in turn, relates to evaluating integrals of the charge density by the following:

$$\bar{g} = \frac{V_{cell}}{(2\pi)^3} \int_{BZ} g(k) dk$$

In order to solve this type of integral numerically, VASP efficiently uses a generating scheme for the k-point grid which was developed by Monkhorst and Pack [48]. If we use the package developed by Monkhorst and Pack, all we have to do is to specify the number of k-points in each direction of the reciprocal lattice, e.g.  $N \times M \times K$ . If there is not a sufficient number of k-points, then the results will not converge well, which implies that before you begin it is a good idea to perform a convergence study. For the simulations run in this thesis, multiple trials were run at variations of increasing k-points and the results were then analyzed in order to see when the increased k-points began to give diminishing returns. If k-points that are too high are selected, the calculation time grows exponentially and it becomes very inefficient to run.

Something else of note that pertains to metals and convergence; there is a discontinuity of the integrands at the Fermi surface, which then divides the  $BZ$  in an occupied and unoccupied section. This essentially implies that in order to have good convergence, one needs a sufficient amount of k-points. There are two well regarded methods used in practice, the tetrahedron method and the smearing method, which are both taken advantage of within VASP. The general idea for the tetrahedron method is to use what is known as a k-grid; this k-grid defines a set of tetrahedra that are filling out the reciprocal space. The function of this method must be integrated and then defined for every point by linear interpolation, which is the simplest case. Without the interpolation of the function, integrating the original space occupied by the set of k-

points; but with interpolation we can integrate the entire space. For everyday use it has been determined that more elaborate interpolation methods have been needed, but the most common method has been developed by Blöchl [49].

In the second method, also known as the smearing method, the discontinuities are “smeared” so that they can be integrated. One example of this smearing is the Fermi-Dirac function.

$$f\left(\frac{k - k_0}{\sigma}\right) = \left[ e^{\left(\frac{k - k_0}{\sigma}\right)} + 1 \right]^{-1}$$

We can replace any step function with a smearing function and evaluate its integral with standard methods. One of the most common methods which is implemented in VASP is the Methfessel and Paxton smearing method [50], which, as it turns out, is more complicated than the Fermi-Dirac function, but conveniently is still characterized by a single variable  $\sigma$



## EVOLUTIONARY ALGORITHM USPEX

Universal Structure Predictor: Evolutionary Xtallography (USPEX) is a method designed around an evolutionary algorithm for structure searches designed by the Oganov group beginning in 2004. USPEX can be used for several different applications such as finding low-energy metastable phases, desired physical/mechanical/electronic properties, stable structures of nanoparticles, surface reconstructions, and molecular packings for organic crystals. The code of USPEX is based on an evolutionary algorithm developed by the Oganov group and has the ability to use alternative methods such as random sampling, meta-dynamics, and corrected PSO algorithms. USPEX has the ability to interface directly with several DFT codes such as VASP, SIESTA, GULP, Quantum Espresso, CP2K, CASTEP, LAMMPS etc.

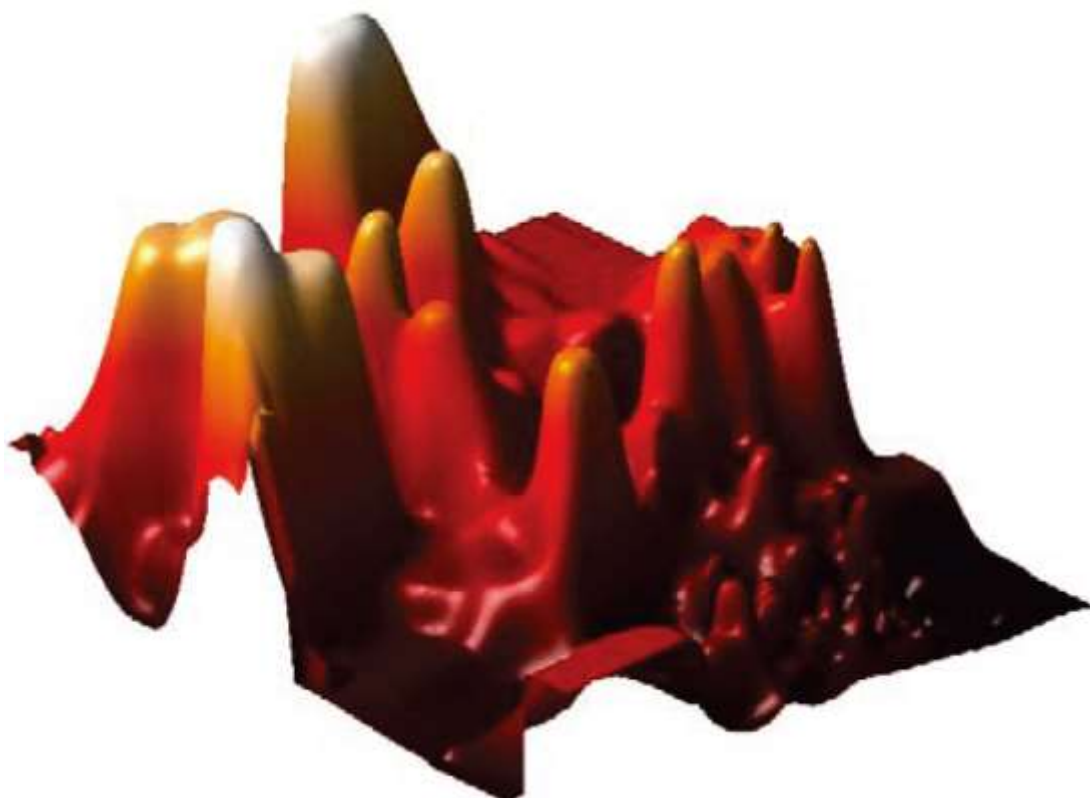


**Figure 7:** A projection of the reduced landscape of Au<sub>8</sub>Pd<sub>4</sub>. It shows clustering amongst low-energy structures in one region.

In Figure 7, an energy landscape has been produced in order to show how USPEX functions. USPEX can scan a landscape from a global perspective finding all energy minimums which can be seen in the visualization. Within the code, USPEX will work in conjunction with VASP to calculate the energies and then determine its hierarchy when compared to the energy of other structures. By this method USPEX can not only find the lowest energy local minimum but also the lowest energy global minimum. Both stable structures and meta-stable structures can also be found by USPEX which the differences can later be resolved with a program like VASP.

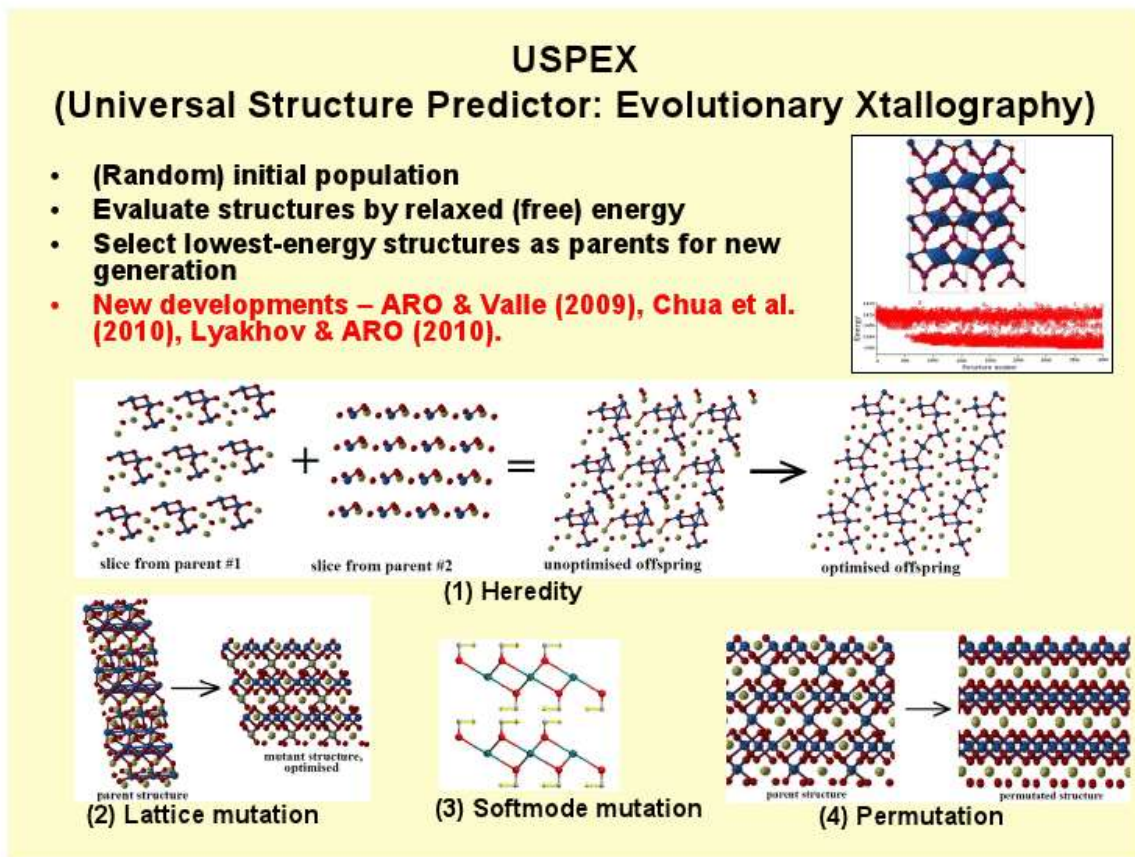


Figure 8: The method in which the evolutionary algorithm alters a parent structure to find the lowest energy

Figure 8 shows the generation method of structures within the evolutionary algorithm. The method begins with a random initial population, and from this population, structures are then energetically relaxed and evaluated to determine the structure with the lowest energy. This lowest energy structure is then taken as the new parent structure and mutated in such a way to allow all possible variations of lattice constants and the beta angle. The energy is then determined from all possible variation structures and this completes one generation cycle within the USPEX system.

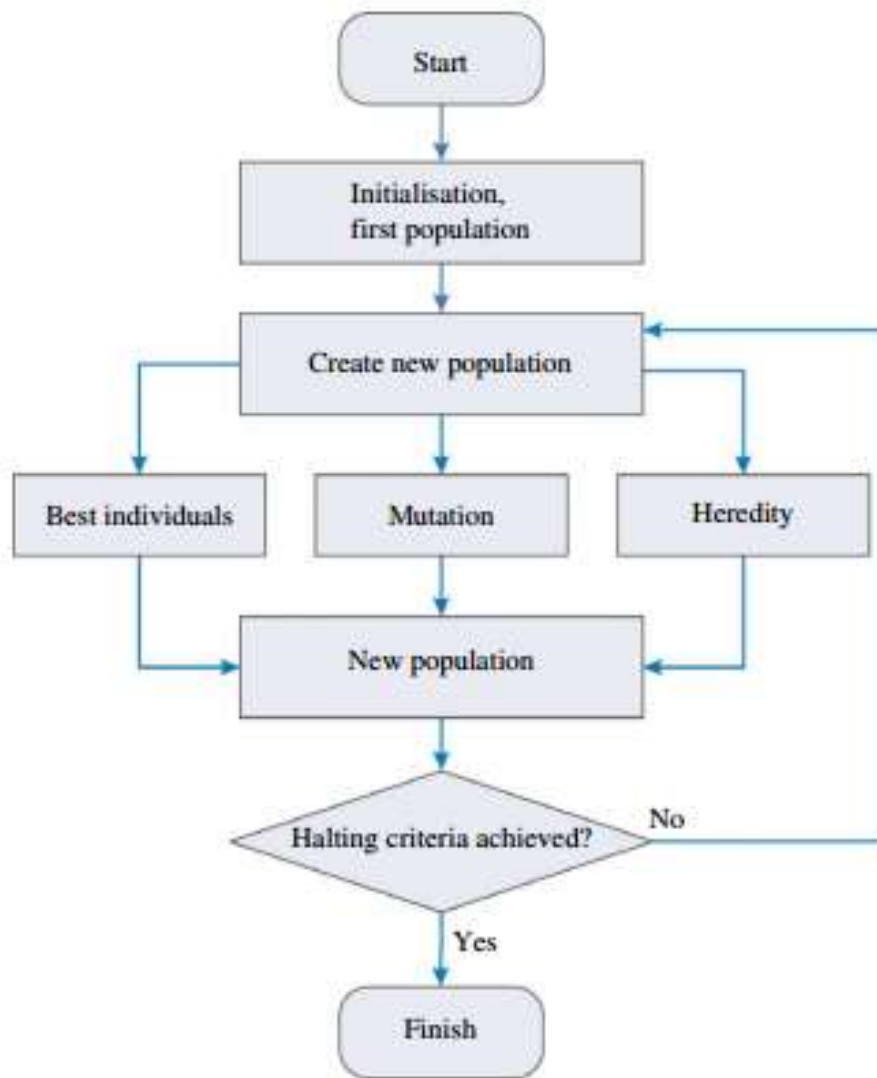


Figure 9: A flow chart of the workings of USPEX

Figure 9 demonstrates how USPEX flows in its variations and the parameters used to determine when the code moves forward. Within the flow chart certain parameters must be determined such as number of generations before completion. In this thesis, the number of generations was determined by testing multiple trials to see when the lowest energy structure had been found repeatedly.

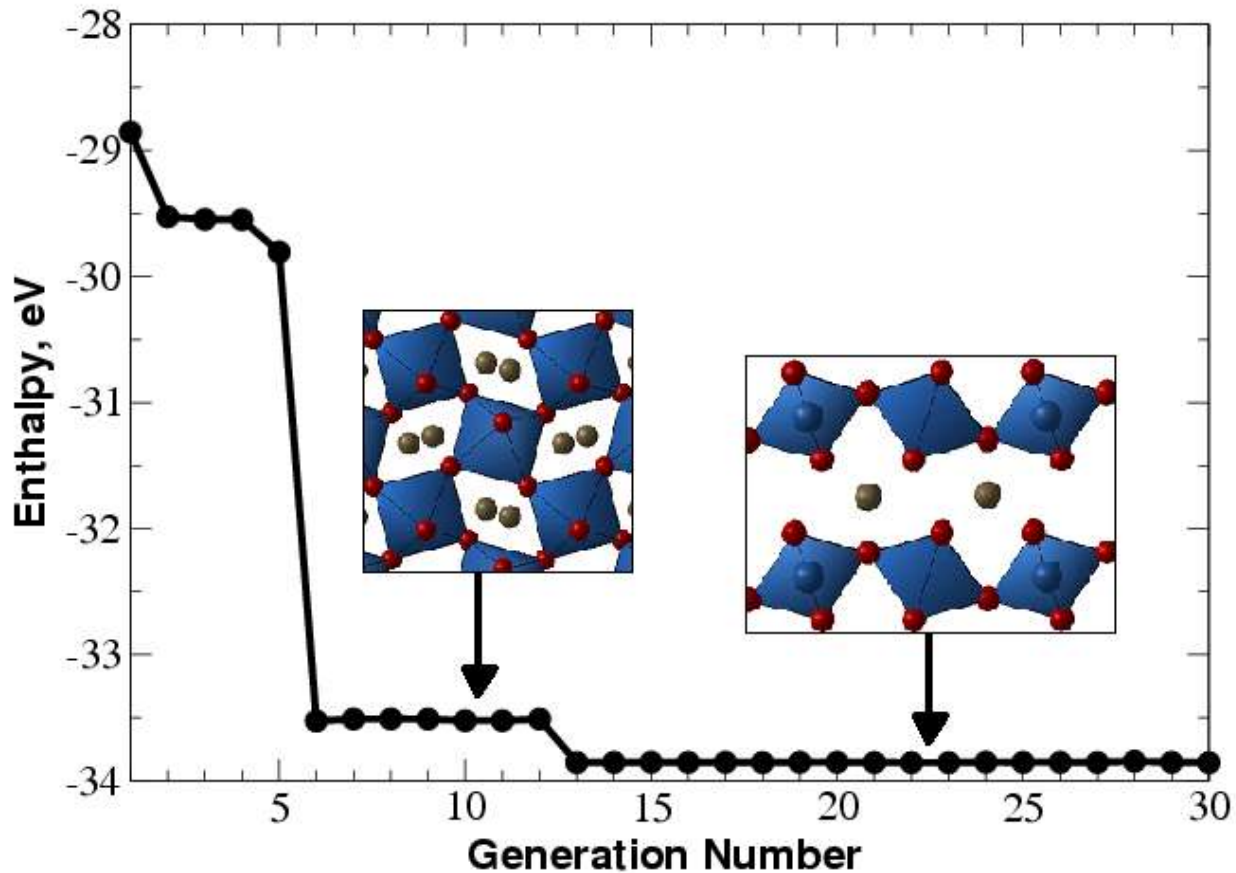


Figure 10: 30 generations showing the enthalpy reduction between each generation.

In figure 10 a particular structure has been selected and is altered over a total of 30 generations. It can be seen that between the 5<sup>th</sup> and 6<sup>th</sup> generation there is a large reduction in the total enthalpy. The structure having a much lower enthalpy appears to be a good selection as the final structure. From this point, it is best to continue searching for new structures using this as the parent structure. We can see over the course of 6 more generations it continues to be the structure

with the lowest energy. However at the 7<sup>th</sup> generation of the algorithm, a new lowest enthalpy has been found. To ensure that the lowest enthalpy structure has been found, it was determined that the generations be carried out 17 more times to a total of 30 generations. For the simulations run for this thesis, 30 generations were also run and successfully found the lowest enthalpy structure well before 20 generations. Thus, for efficiency, all structure searches were run for 20 generations.

# CHAPTER 3

## STRUCTURAL MODEL AND METHODS OF CALCULATIONS

For the searches of stable compounds and structures, the evolutionary algorithm USPEX [50-53] was used. *Ab initio* structure relaxations were used in conjunction with the USPEX evolutionary algorithm and based on density functional theory (DFT) using the local density approximation method to find the exchange correlation functionals and implemented within the program VASP [54]. For our simulations we ran the USPEX structure search for 30 generations; we then tested the same simulations at 20 generations and consistently came up with the same results. We determined that 20 generations was sufficient to confidently find the lowest energy state. We used increments of 50 GPa from 0-300 GPa in our structure searches using USPEX. As we decided to only analyze the energies up to 150 GPa, we found our highest phase change of calcium at 112 GPa. The electron projector-augmented wave (PAW) method was used for structural relaxation with a plane wave basis set using a kinetic energy cutoff point at 700 eV which gave good convergence of stress tensors. We performed simulations upwards of 900 eV with approximately the same results, but the simulations took a great deal more time to calculate. For the Brillouin zone, which was sampled by the Monkhorst-Pack meshes, we used a k-mesh of 888 which gave a similar description of the previous experimental and theoretical work done on elemental calcium, oxygen and the compound calcium oxide (Ca, O, and CaO respectively). Again, we ran our simulations up to  $12 \times 12 \times 12$  but our results ended at a similar level as the results given by the  $8 \times 8 \times 8$  simulations. The calculations were checked upon completion to make sure that a force convergence criteria of  $10^{-2}$  meV and that the energy convergence criteria was also  $10^{-2}$  meV. Our composition space was described by  $[\text{Ca}_x\text{O}_y]$ , which provided USPEX a way to search over a wide range of possible compositions. Any composition not included in

this study was left out because it was found to not be predicted by USPEX or not be thermodynamically stable. This also gave us a method of searching a desired composition if it was of particular interest. For the correlation and exchange functionals we used the local-density approximation method (LDA) [55] which gave us the most accurate results compared to a laboratory environment.

# CHAPTER 4

## RESULTS AND DISCUSSION

In order to determine the various characteristics of Ca-O compounds, we first needed to determine the properties of its constituents, calcium and oxygen. Our goals included creating a stoichiometry graph and calculating the formation energy of various Ca-O compounds; in order to do this, we would first need to determine the phase boundaries of calcium and oxygen. Also, because calcium is so well studied, we can use the results from this element as a benchmark of the system we are using in order to determine the accuracy of our results. We began with discovering the phase boundaries of calcium using the LDA DFT method and the use of VASP.



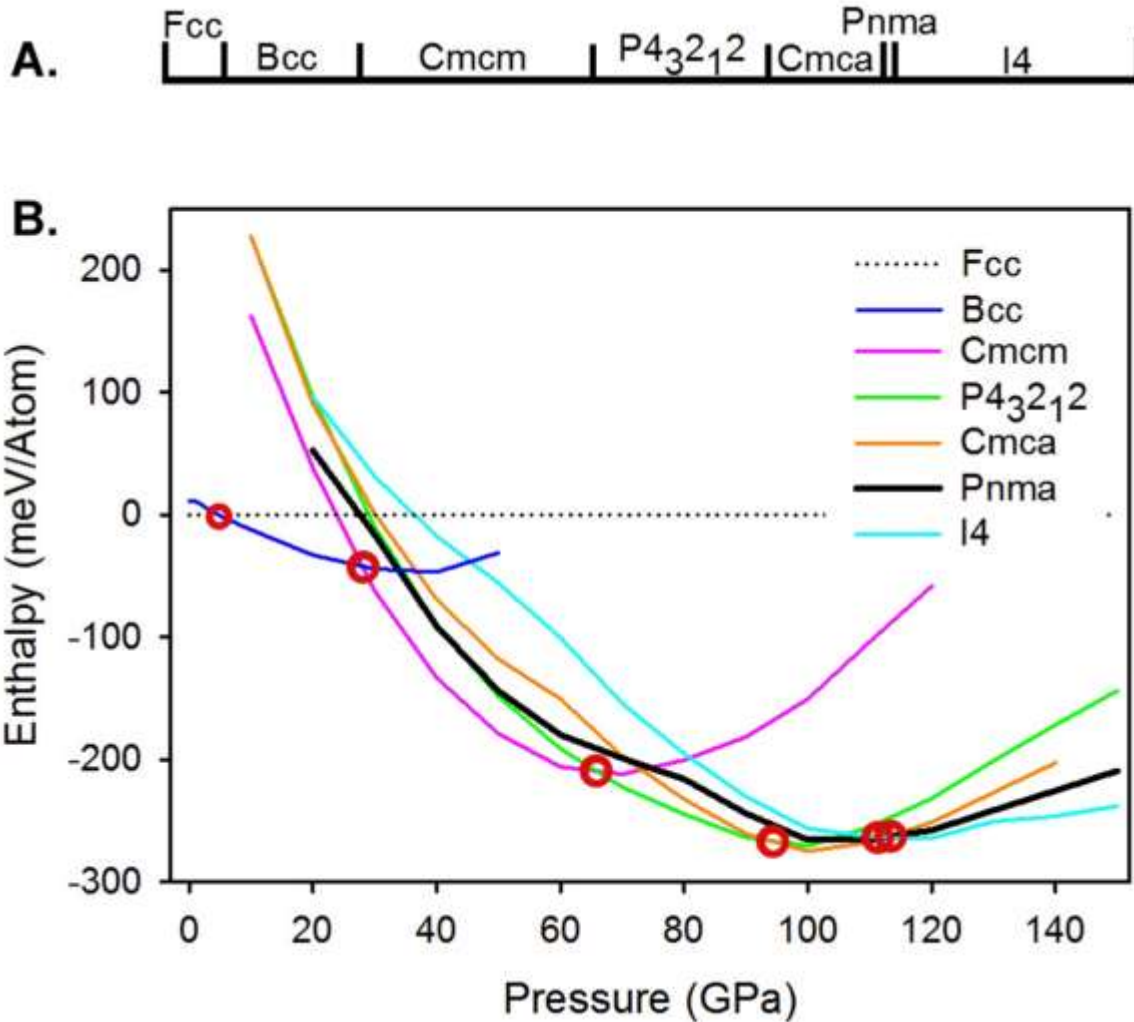


Figure 12: We found 7 stable phases up to 150 GPa which can be seen in Figure 12.A. In Figure 12.B. it can be seen at what pressure the phase changes occur which is indicated by the open circles.

In Figure 12.A we can see the 7 phases of calcium that were found from our simulations and the corresponding pressures which match with Figure 12 B. In Figure 12 B we show the approximate pressure in which a phase change occurs. The phase transition of Ca-I to Ca-II is the Fcc to Bcc phase; we found this transition to happen at 4.7 GPa. This agrees with other theoretical simulations which resulted in the phase transition occurring at 3.5 GPa [9]; experimental results have found results in the area of 20 GPa [56]. From Ca-II to Ca-III is the Bcc to Cmcm phase which transitions at 28 GPa. Comparing to other theoretical simulations of 32 GPa it is again

reasonably close [9]; experimental values agree well, as they too find the transition pressure to be 32 GPa [56]. Ca-III to Ca-IV is the Cmcm to P4 transition and happens at 66 GPa. Comparing once again to other theoretical simulations we determined the pressure of the transition phase to be at 74 GPa [9]. Experiments found this transition at slightly higher pressures of 113 GPa [56] and 119 GPa [10]. From Ca-IV to Ca-V we see the P4 structure and the Cmca structure transition at 94 GPa. Similar theoretical simulations found this transition pressure to be at 109 GPa [9] and experimental results once again have a higher transition pressure of 143 GPa [10]. The phase transition from Ca-V to Ca-VI commenced with the Cmca structure and transitioned to the Pnma structure at 111 GPa. In other theoretical works, the transition was determined to take place at 117 GPa [9] and experimentally, the transition has been observed to take place at 172 GPa [57]. And finally we found Ca-VII, I4 very close with Ca-VI at 112 GPa; which again comparing to other theoretical work of 135 GPa [9]. Experimentally however we find this transition pressure to be higher occurring at 210 GPa [57].

Compound	Pressure (GPa)	a (Å)	b (Å)	c (Å)	$\alpha$	B	$\Gamma$	Space Group
Ca <sub>2</sub> O <sub>3</sub>	40	7.01	5.63	6.07	90.00	127.92	90.00	C2/c
CaO <sub>2</sub>	40	4.66	4.19	5.47	90.00	90.00	90.00	Pnma
Ca <sub>2</sub> O <sub>3</sub>	90	3.64	3.83	6.29	90.00	115.39	90.00	C2/m
CaO <sub>2</sub>	90	3.94	3.97	5.46	90.23	82.35	89.88	P21c
Ca <sub>2</sub> O <sub>3</sub>	150	2.54	2.54	6.08	106.92	106.92	93.14	I4/mmm
CaO <sub>2</sub>	150	3.90	3.90	3.90	117.36	125.63	87.59	P21c
CaO <sub>3</sub>	150	4.42	4.45	2.67	90.13	90.09	90.01	P-421
CaO low phase	40	4.42	4.42	4.42	90.00	90.00	90.00	Fm-3m
CaO high phase	90	2.56	2.56	2.56	90.00	90.00	90.00	Pm-3m
CaO high phase	150	2.47	2.47	2.47	90.00	90.00	90.00	Pm-3m

**Table I: A table of the particular compound, pressure, lattice constant, lattice angle, and space group run in simulations.**

Table 1 displays a list of compounds with a particular structure that are energetically stable. Within this table, the lattice constants for that particular compound and structure are listed along with the transition pressure it was achieved at. Simulations for elemental oxygen were conducted from 0-150 GPa. The evolutionary algorithm USPEX was used to find the various phases of oxygen and resulted in 4 predicted phases, alpha, delta, epsilon and zeta. Again, 30 generations were run as a test and then reduced to 20 generations in USPEX for efficiency. VASP was then used for structure relaxations, the determination of phase boundaries, and total enthalpy. Oxygen required the use of higher energy cutoffs in order to be certain of its accuracy. 16 atoms were used per calculation at an 800 eV cutoff and an 8x8x8 k-mesh. It has recently been shown that solid oxygen takes on the form of an O<sub>8</sub> molecular lattice [58], and thus, our model was created with this idea in mind. This model focuses on the association of four O<sub>2</sub> molecules formed into a

rhombohedral molecular unit and hence the total of 8 oxygen atoms. The bonds that hold this structure together are attributed to be chemically weak in nature. The epsilon phase has been shown experimentally to transition into the zeta phase at 96 GPa and to metallize at this pressure [59-61]. Our simulations predicted the epsilon-zeta transition to occur at 97 GPa, which is in good agreement with the experimentally determined transition pressure. We have observed a phase transition from the alpha phase to the delta phase at 5.76 GPa. It has also been shown experimentally that there is a volume collapse before the delta phase, our simulations confirm this volume collapse [62]. The phase transition from the delta phase to the epsilon phase has been difficult to determine due to the enthalpy difference being very small and the limiting accuracy of the LDA DFT method. In another theoretical simulation, it has been shown that the generalized gradient approximation (GGA) has given reasonable results when compared to experiment at lower pressures [63], but the method still has trouble distinguishing the enthalpy differences at various other pressures. Of all the diatomic molecules, currently the only one known to have a magnetic moment is oxygen. Within the solid oxygen molecule, it is this inherent magnetic moment that affects the accuracy of the LDA method. This magnetic effect becomes minimal as pressure increases and seems to all but dissipate as the epsilon phase begins. The magnetic order was observed to be destroyed with the formation of the epsilon phase [64]. By 17 GPa, this effect is no longer an issue and the accuracy of the LDA method begins to agree well with experiment. At lower pressures within the epsilon phase, our simulations showed excellent agreement with experiment. In one experiment, the pressure of 17.6 GPa was studied thoroughly [58], and reported the shortest O-O bond lengths at 1.21 Å and the longest O-O bond length to be 2.19 Å. Our simulations for comparison were run at 17.6 GPa and showed the shortest bond length to also be at 1.21 Å. The longest O-O bond length within our simulation

measured 2.05 Å. In Figure 13, a visualization has been created to show the two bond lengths within the O<sub>8</sub> oxygen structure. Using the lattice parameters given within the experimental work, a simulation was performed comparing enthalpies of the relaxed structures. Using the experimental parameters resulted in a calculated enthalpy of -4.64026 eV per atom compared to our modeled simulation enthalpy of - 4.63981 eV per atom. For the remaining pressures, enthalpies were calculated in the same manner using VASP calculations.

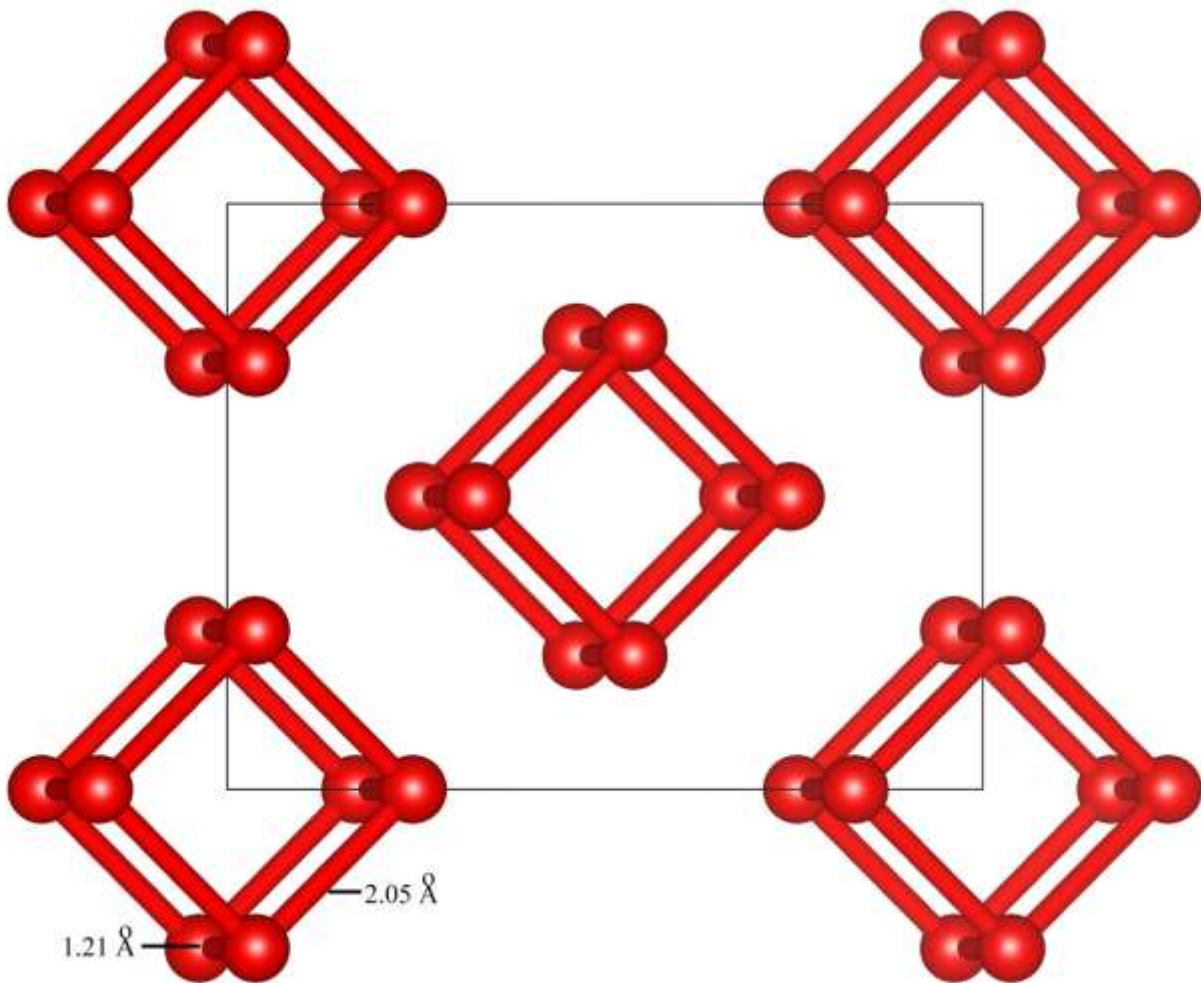


**Figure 13: An O<sub>8</sub> oxygen structure scheme was adopted for our modeling. The O-O bond distance has been labeled for comparison against experimental work**

We used the evolutionary algorithm USPEX for our structure search. We tested within the program from 0 GPa to 300 GPa in 50 GPa increments. In Figure 14 we see a pressure-

composition phase diagram compiled from the results of our structure search. The diagram was constructed by calculating the enthalpies (i.e., the zero temperature free energy ( $E + PV$ )) of the elements and finding the phase boundaries. In these calculations we simply found the phase boundaries, but another calculation is needed in order to determine whether or not the structure is stable or meta-stable. In our structure search we performed calculations up to 300 GPa, however the structures remained the same above 200 GPa within the confines of our simulations. All structures were fully relaxed by finding a local minimum in the structure search. Our calculations for CaO find the transition from B1 to B2 at 58 GPa, which is in good agreement with not only experimental results, but also other high pressure, zero temperature simulations [2,65,66,67]. For the composition  $\text{CaO}_7$ , we predict 3 phases of which the two phase transitions occur at 47 GPa and 102 GPa. Our next composition was  $\text{CaO}_3$ , in which we found 3 phases. The phase transitions for  $\text{CaO}_3$  occur at 22 GPa and 51 GPa.  $\text{CaO}_2$  was our third composition in which we found 3 phases, each of which have phase transitions at 28 GPa and 91 GPa. Our next studied composition was  $\text{Ca}_2\text{O}_3$  in which we found 4 phases. The phase transitions for this chemical composition were found at 10 GPa, 70 GPa and 118 GPa.  $\text{Ca}_2\text{O}$  was found to have 3 phases and 2 phase transitions at 28 GPa and 93 GPa. The composition of  $\text{Ca}_3\text{O}$  was observed to have 4 phases with phase transitions at 25 GPa, 70 GPa and 195 GPa. Our last tested chemical composition was  $\text{Ca}_7\text{O}$  which we see to have 3 phases of which had phase transition pressures of 22 GPa and 55 GPa.

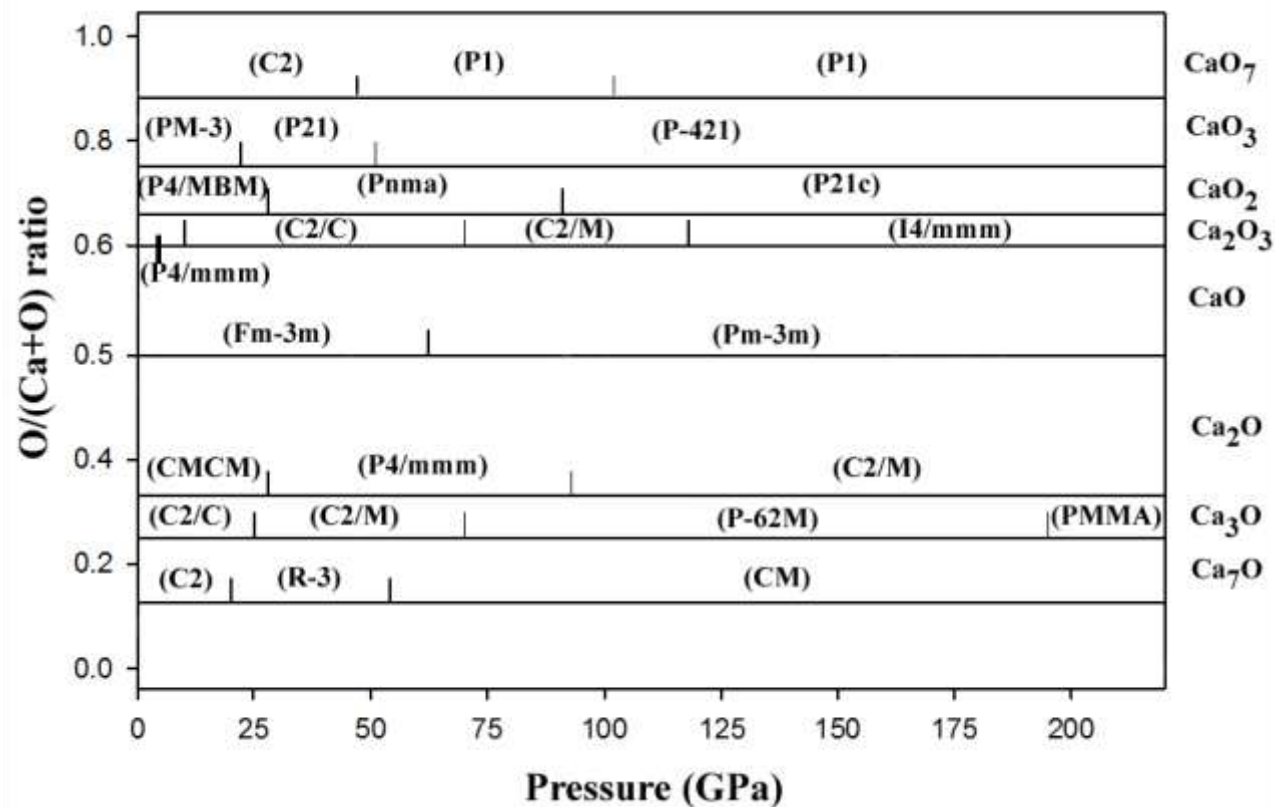
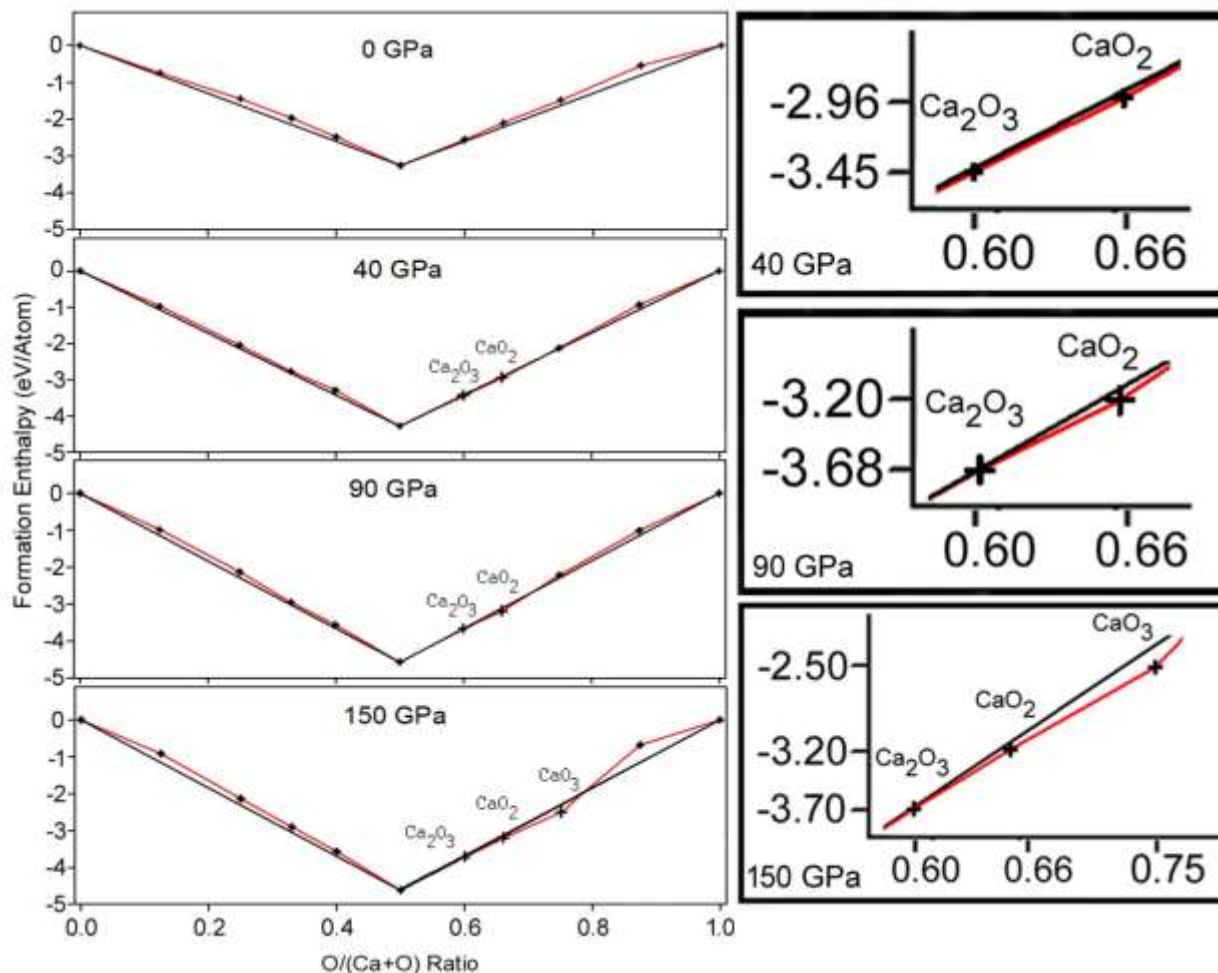


Figure 14: A pressure-composition phase diagram of calcium, oxygen and its various chemical compositions up to 225 GPa. Our structure search ran up to 300 GPa, however, we found no new changes above 200 GPa.

In order to figure out whether or not a structure was stable or meta-stable we needed to first calculate the formation enthalpy of both calcium and oxygen. Once the constituent pieces of our initial focus, CaO, had been calculated, we then calculated the formation enthalpy for the compound CaO itself. Determining the path that the enthalpy would most likely take in order to get to the lowest energy state, we could then introduce our newly calculated formation of enthalpies in order to find out if the new structures were more stable than the formation of CaO itself. Although calcium itself has only 2 valence electrons, at higher pressures the inner core electrons will become available and at certain pressures more preferable. This phenomenon can result in the formation of compounds that are not in a 1:1 ratio. Via our calculations, we did find many meta-stable structures and 3 new stable structures as shown in figure 15. For the purposes

of this study, all calculations were made at zero kelvin temperatures, which may account for some, if not all of the discrepancies between our results and experimental results.



**Figure 15: A Stoichiometry plot showing the latest stable compounds in their lower energy states. The first stable compounds can be seen at 40 GPa and are represented by circles. These compounds remain stable at 90 GPa and 150 GPa with an additional new compound appearing at 150 GPa. Metastable compounds are represented by plus symbols. The black line represents the line of stability where CaO can be found, the red line is the calculated formation energy of the compounds tested.**

In Figure 15, we present a stoichiometry plot showing the new stable structures under high pressure. Each high pressure phase was calculated using the corresponding phase of calcium in conjunction with the calculated elemental oxygen. The first appearance of a newly stable structure occurs at 40 GPa with the compounds Ca<sub>2</sub>O<sub>3</sub> and CaO<sub>2</sub>. The compounds remain stable up to 150 GPa which is the maximum pressure that was tested. At 150 GPa we also found a new



stable structure for the first time,  $\text{CaO}_3$ . At 40 GPa,  $\text{Ca}_2\text{O}_3$  can be found at -3.45 eV, CaO can be found at -3.42 eV at the same pressure with a difference of 30 meV. Making the approximation that 1 eV is 11,600 kelvin through the equation  $E = k_B T$ ; this places the difference at about 300 kelvin.  $\text{CaO}_2$  at the same pressure of 40 GPa can be observed at -2.96 eV with the stable compound of CaO at -2.91 eV and a difference of 50.0 meV. Again making a temperature approximation, this places the difference at about 500 kelvin. At 90 GPa we have the same two stable compounds,  $\text{Ca}_2\text{O}_3$  at -3.68 eV and its normally stable counterpart CaO at -3.66 eV with a difference of 20.0 meV, which approximates the temperature to be about 200 kelvin.  $\text{CaO}_2$  we calculated to be at -3.20 eV and CaO at -3.11 eV put under the same pressure with a difference of 90.0 meV. This places our temperature estimate at 900 kelvin. At 150 GPa we found our new stable compound of  $\text{CaO}_3$  at -2.50 eV and CaO at -2.31 eV with a difference of 190 meV. This was our largest difference and equates to the highest temperature which is approximately 1900 kelvin.  $\text{CaO}_2$  at 150 GPa was found to have an energy of -3.20 eV and CaO at -3.14 eV with a difference of 60 meV. Finally we have  $\text{Ca}_2\text{O}_3$  at 150 GPa with an energy of -3.71 eV and CaO with an energy of -3.69 eV and a difference of 20 meV and finally a temperature approximation of 200 kelvin. The phases for CaO itself that were found are very high symmetry phases and match what we naturally see occurring in nature. As for the other compositions, they are in fact lower symmetry, but they do have order within the systems that make up the space groups.

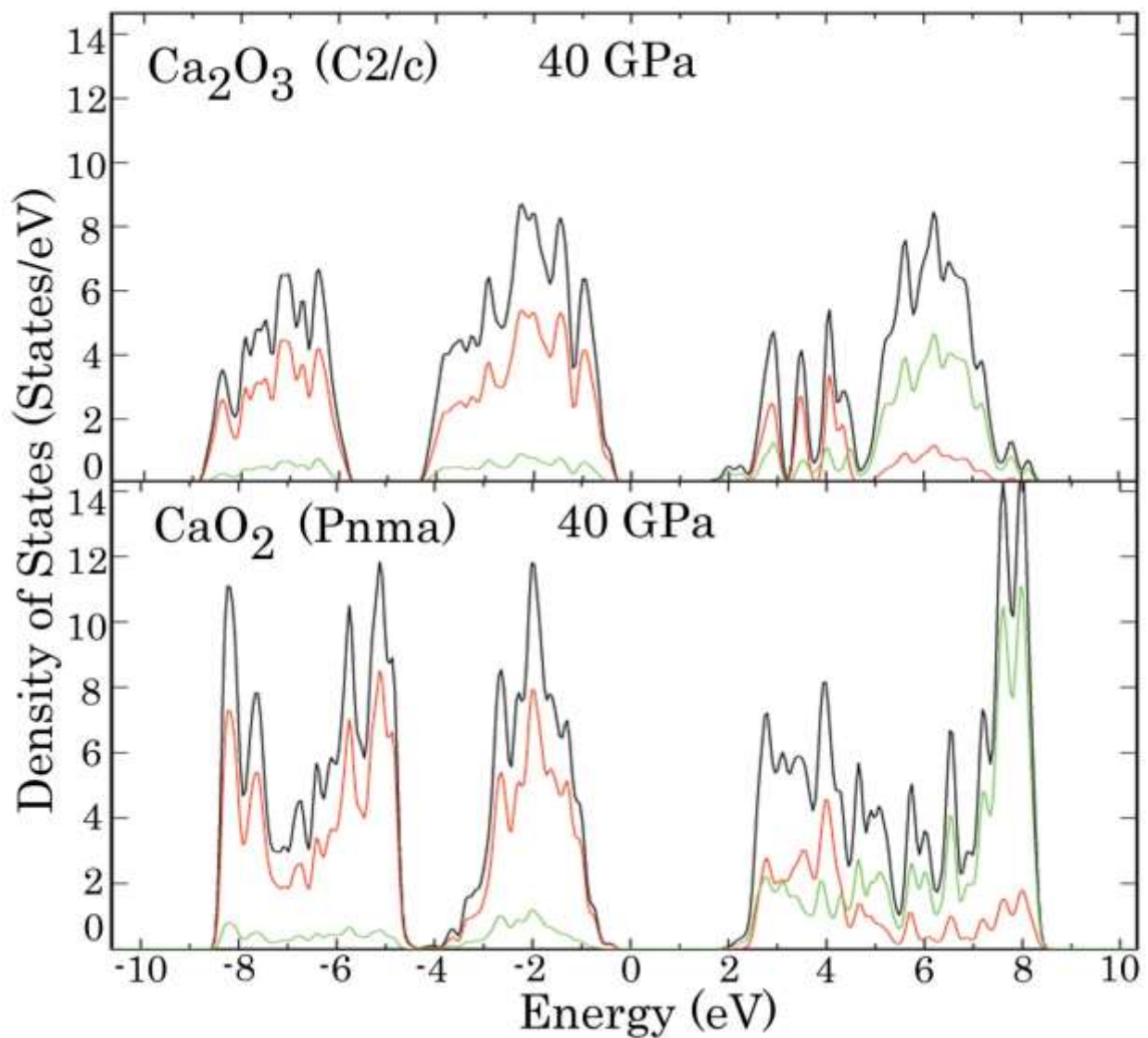


Figure 16: Density of states plots for new stable compounds at 40 GPa. An energy gap can be seen indicating an insulating structure. The red line indicates the oxygen contribution, the green line represents the calcium contribution and the black line represents the calcium contribution and the black line represents the total for all orbitals.

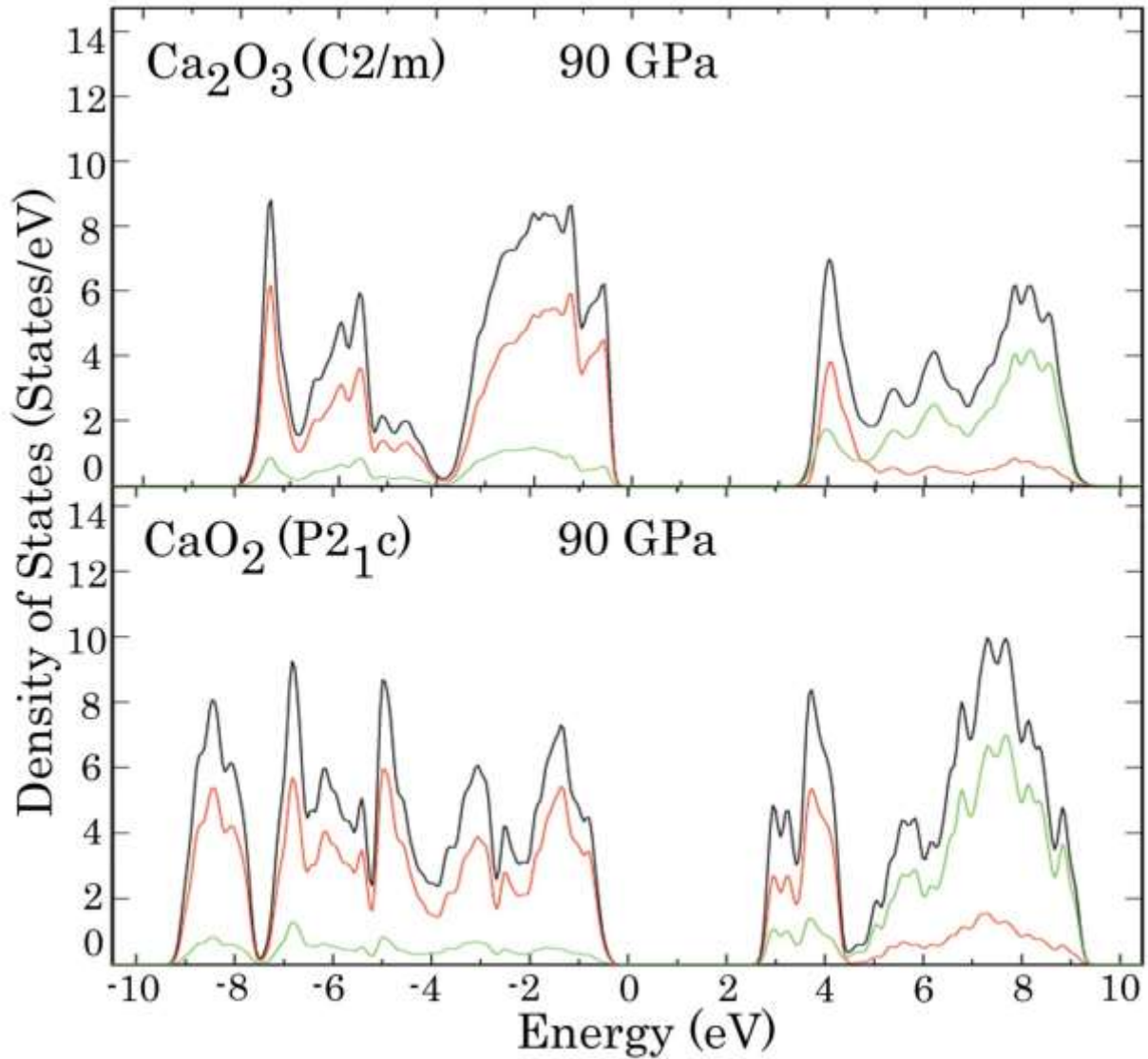


Figure 17: Density of states plots for new stable compounds at 90 GPa. An energy gap can be seen indicating an insulating structure. The red line indicates the oxygen contribution, the green line represents the calcium contribution and the black line represents the calcium contribution and the black line represents the total for all orbitals.

We present the density of states plots for the new stable structures,  $\text{Ca}_2\text{O}_3$  and  $\text{CaO}_2$  that appear at 90 GPa. In Figure 17, the black line is the combination of the oxygen contribution and the calcium contribution for each compound; the red lines represent oxygen and the green lines calcium. It can be seen that a gap above the Fermi level clearly indicates that the compounds have remained insulators at 90 GPa. At both ends of the gap that the oxygen contribution dominates.

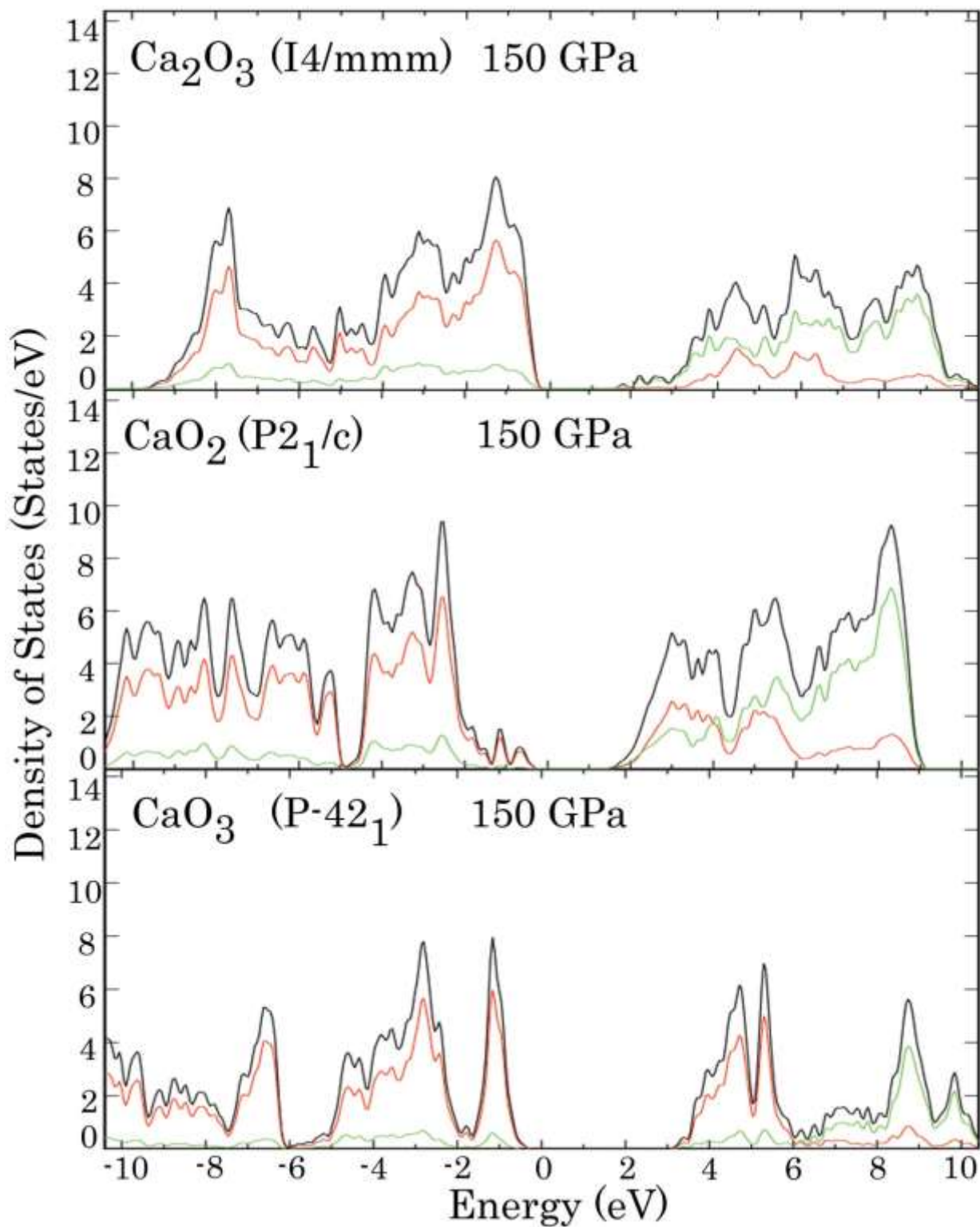


Figure 18: The density of states plots for newly found stable compounds at 150 GPa. An energy gap can be seen in all 3 compounds indicating an insulating structure. The red line indicates the oxygen contribution; the green line represents the calcium contribution and the black line represents the total for all orbitals.

In Figure 18 we display the density of states plots for newly stable structures at 150 GPa. Both  $\text{CaO}_2$  and  $\text{Ca}_2\text{O}_3$  remain stable with a new addition of  $\text{CaO}_3$ . However, a trend can be noted in the reduction of the band gap; at 90 GPa  $\text{Ca}_2\text{O}_3$  has a gap of 3.75 eV and has a significant reduction down to 1.71 eV.  $\text{CaO}_2$  is also observed to be at 3.28 eV and is reduced to 1.21 eV moving closer to becoming a semi-conductor. We can see that for  $\text{CaO}_3$  that the oxygen contribution dominates both sides of the gap, which may or may not change as pressure increases. For our  $\text{CaO}_2$  however, we can see that above the Fermi level the oxygen contribution is no longer the dominating contribution; calcium and oxygen seem to be equal contributors. For  $\text{Ca}_2\text{O}_3$  a similar trend as  $\text{CaO}_2$  is observed, however, in this case not only has the calcium contribution increased, it is now dominating the oxygen contribution.

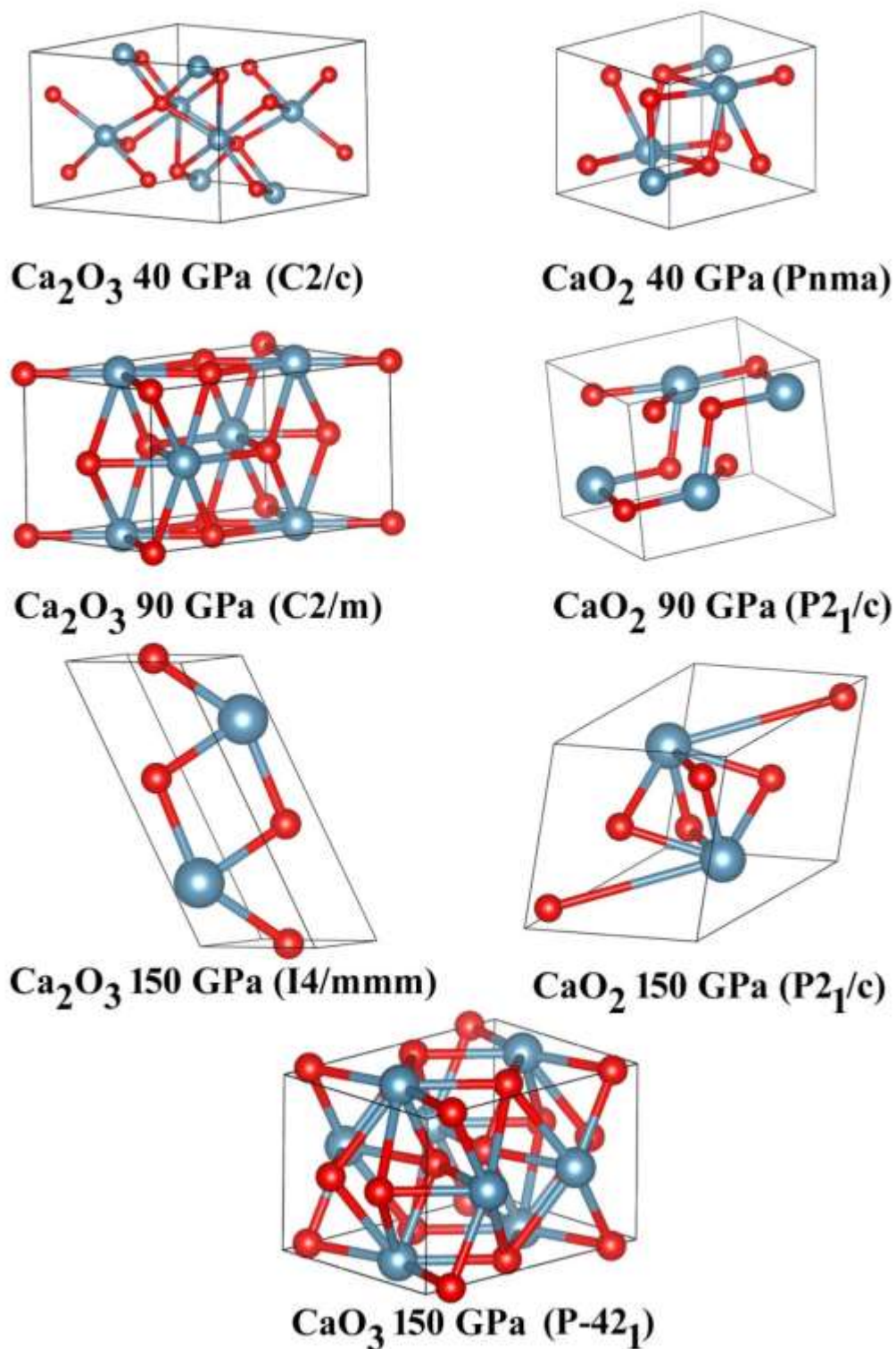


Figure 19: Crystal structures of the new stable compounds under high pressures. Calcium molecules are represented by red spheres and oxygen molecules are represented by blue spheres.



## INTRODUCTION

In this work, we also explore the crystal structure of  $\text{Li}_2(\text{OH})\text{Br}$  which has shown promise for an application as a solid electrolyte material in Li-ion batteries [68]. The initial goal of this project entailed properly modeling the crystal structure in order to largely understand ionic transport properties and any additional properties the compound may have. Upon finding adequate crystal structure candidates, we then simulated the x-ray diffraction patterns by way of the program Mercury® using copper K-alpha radiation in order to simulate the conditions that were used in the experimental procedure [69]. We then investigated the pressure-volume equation of state, electronic density of states, and phonon density of states to further characterize these key properties that are vital to understanding the ionic transport properties, which are crucial to the battery applications.

## STRUCTURAL MODEL AND METHODS OF CALCULATION

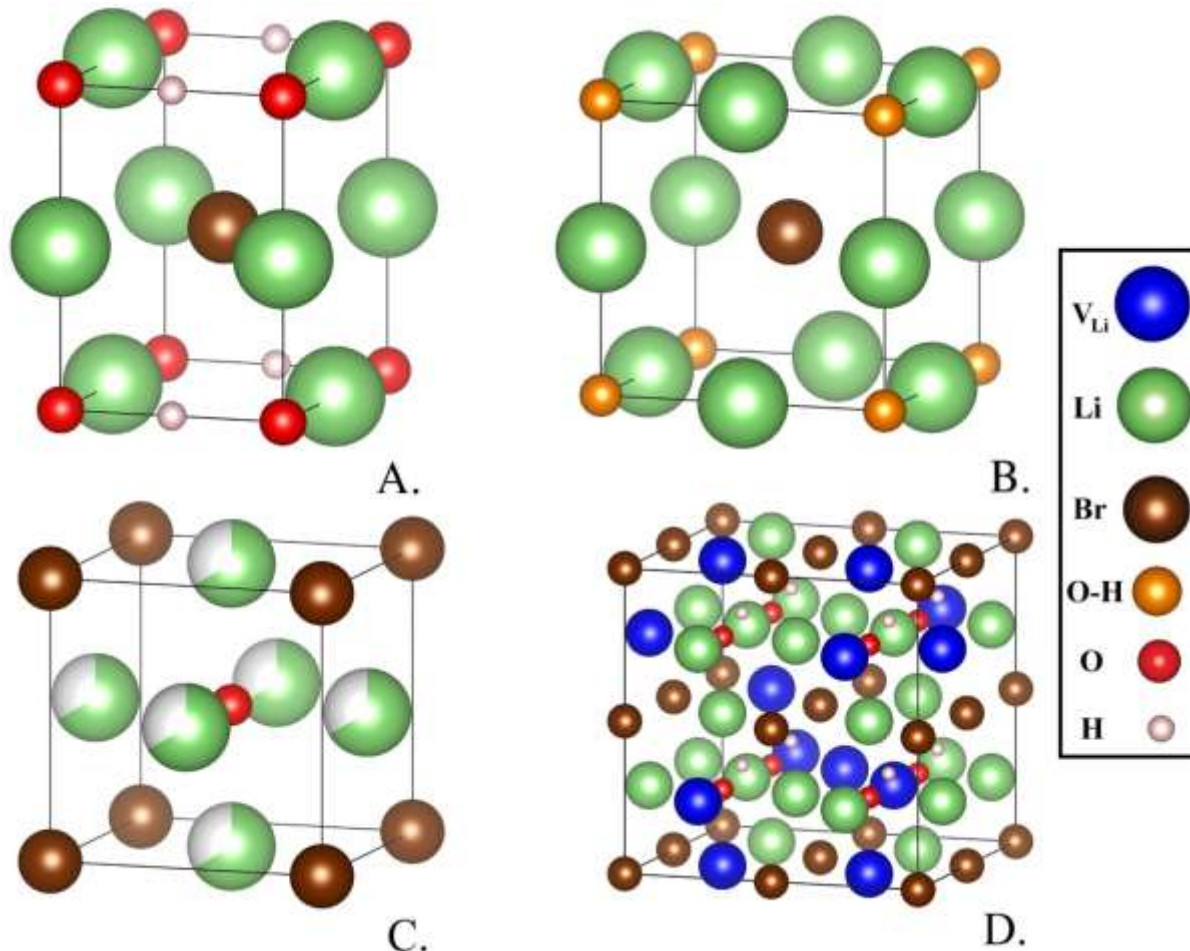


**Figure 20. Various candidate crystal structures. A, B: Two variations of the primitive unit cell. C. A structure with fractional occupation originally proposed based on experimental results. D. A supercell model built to accommodate the unique lithium vacancy ( $V_{Li}$ ) structure proposed in the present work.**

In Figure 20 we propose 4 crystal structure candidates with various atoms labeled by color and size. If we begin by looking at figure 20, a crystal structure that was originally proposed based off Rietveld refinement from experimental x-ray diffraction (XRD) data taken from the first time the compound was analyzed [68]. This model proposed that there was an ionic spatial occupancy for the lithium sites that resulted in them filling the sites fractionally by  $\frac{2}{3}$  of the time. The hydrogen atoms were determined to not significantly influence the structure so they were excluded from this particular model. The model fits the experimental data quite well and there is



little disagreement that it is correct at this time. When attempting to recreate this model within the confines of DFT calculations using the VASP software, a challenge became apparent when trying to model the ionic spatial occupancies because thus far, VASP has not been designed to carry out this task [70]. An initial attempt was made, as seen in figure 20.A using the crystal database file based on the experimental model. The LDA method was used with a K-mesh of  $8 \times 8 \times 8$  was used along with a plane wave cutoff energy of 900 eV for the parameters in VASP for the structural relaxation. The calculations were checked upon completion to make sure that a force convergence criterion of  $10^{-2}$  meV was met and that the energy convergence criterion was also  $10^{-2}$  meV. The actual compound is known to be a cubic structure; however, the energetic relaxation calculation resulted in a tetragonal structure which, in the end was too much of a difference when comparing XRD patterns from this structure to the realistic one found by experimentalists. A second attempt was made by trying to find the actual experimental space group of 221, which is Pm-3m. This attempt can is shown in figure 20.B in which the appropriate atoms were placed into the structure and then forced into the space group 221 in order to see how the configuration must end up to fulfill this requirement. The structure resulted in some interesting aspects such as the placement of the hydrogen atoms directly on top of the oxygen atoms, simulating something close to what was proposed in the model based off of experimental results. It could clearly be seen though that the structure was not correct at the very least because of the lithium atom placement. Thus, a new method had to come about in order to properly model this compound. The method I have worked out involves creating a supercell large enough that vacancies could be introduced by removing lithium atoms from particular spaces. A 40 atom cell was initially created with the appropriate amounts of each atom in order to reproduce the correct unit cell. From there, 8 lithium atoms were removed in order to recreate an ionic vacancy

scheme that represented the approximate 66% lithium occupancy in the experimental model. The lithium vacancy sites were chosen specifically to reproduce a real world approximation; each lithium vacancy site was not placed within a nearest neighbor range or adjacent to another lithium vacancy site. There are actually two different variations of this that can occur; both were created and the model with the lowest energy state was then chosen as the more appropriate structure.

## RESULTS

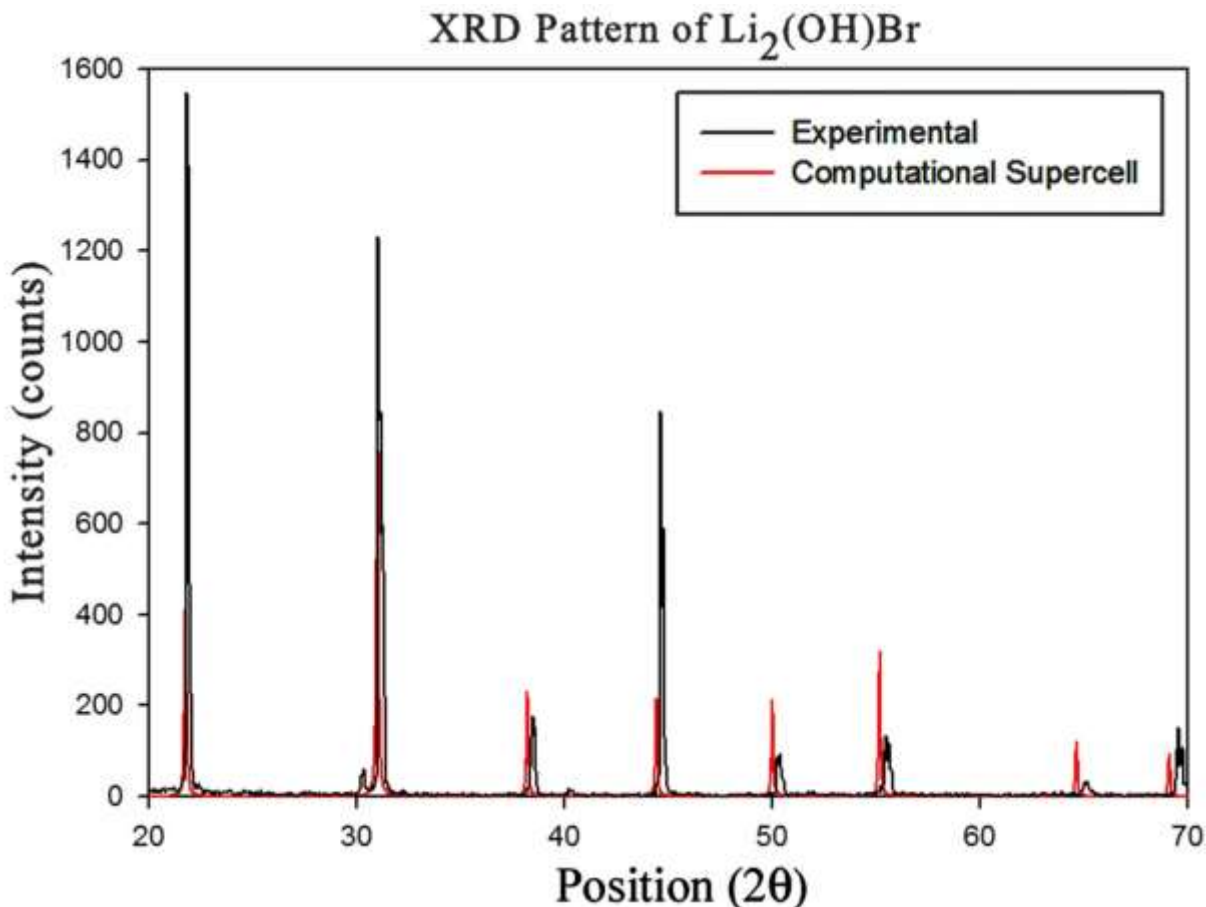


**Figure 21. Comparison of simulated x-ray diffraction patterns of the supercell model (Fig. 5D) compared to the experimental x-ray diffraction spectra of  $\text{Li}_2(\text{OH})\text{Br}$ .**

In Figure 21, an experimental XRD measurement was carried out in the lab at UNLV and is represented by the black line [71]. The red line was created by taking the newly created 40 atom supercell and subjecting it to an XRD simulation within the program Mercury. The simulated XRD used the parameters that mimic the copper K-alpha radiation that was used to obtain the experimental results. Within these results it can be seen that the comparison is very close with a slight shift in the position angle. There are several reasons that could possibly account for this shift; the first involves the fact that LDA generally underestimates the cell volume which would

certainly skew the results in a certain direction. This direction, however, would displace the plot to the right. The second possible reason is the fact that these simulations are run at zero kelvin, which would also underestimate the cell dimensions and again displace the cell to the right. A third problem that could account for this shift is the fact that the supercell is simply too small too properly simulate the correct experimental model. If the sample size of the lithium vacancy sites were greater, this would replicate real world results in a more accurate manner. It can still be determined that the modeling method has reproduced a pretty accurate crystal structure that resembles the original experimental model. In the future, the unit cell may be expanded to greater size requiring a great deal more computational power and time, but at the time of writing this thesis, this next step has yet to be carried out.

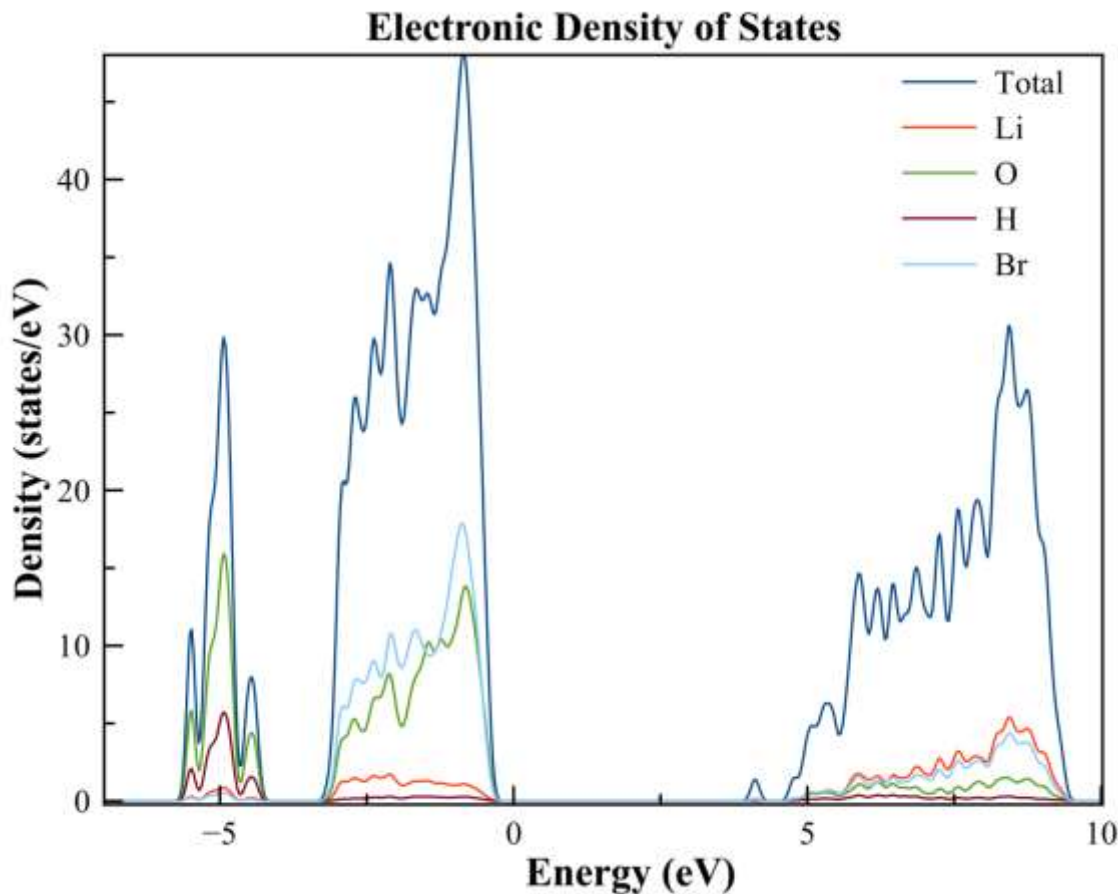
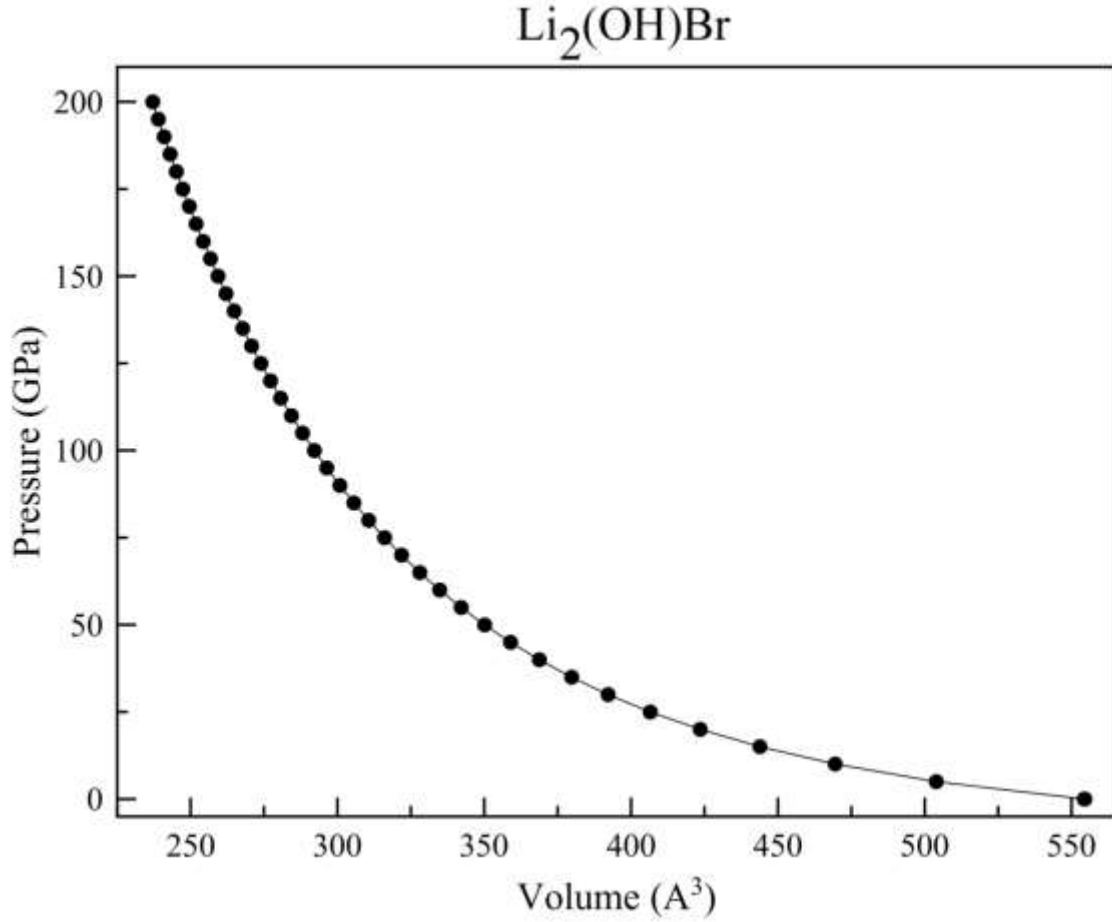


Figure 22. Calculated total electronic density of states of the supercell model of  $Li_2(OH)Br$  (dark blue lines) and partial density of states from each element as indicated by the colored lines.

In Figure 22, we present an electronic density of states plot that also includes the partial density of states of each atomic contribution. From this plot, the band gap can be measured to approximately 4 eV. A similar material can be used for comparison,  $Li_3OBr$  which should make for a good approximation since it is also a cubic structure that has lithium as a metal within it [72]. So when comparing  $Li_3OBr$  with  $Li_2(OH)Br$  we can note that their respective band gaps are 4.8 eV and approximately 4.0 eV.



**Figure 23.** Calculated pressure-volume equation of state of  $\text{Li}_2(\text{OH})\text{Br}$ , producing a bulk modulus of 49.6 GPa via a fit.

In Figure 23, we present a volume-pressure curve from 0 to 200 GPa. The curve was produced by again using DFT calculations via VASP. For these calculations, a K-mesh of 4x4x4 was used for efficiency with a higher plane wave cutoff energy of 900 eV. The LDA method was again used for this portion of the project. From these calculations we were also able to calculate the bulk modulus via the Birch-Murnaghan equation of state. Where the equation is based off the pressure  $P$ , the reference volume  $V_o$ , the deformed volume  $V$ , and the bulk modulus represented by  $B_o$  which in turn appears as:

$$P(V) = \frac{3B_o}{2} \left[ \left( \frac{V_o}{V} \right)^{\frac{7}{3}} - \left( \frac{V_o}{V} \right)^{\frac{5}{3}} \right] \left\{ 1 + \frac{3}{4} (B'_o - 4) \left[ \left( \frac{V_o}{V} \right)^{\frac{2}{3}} - 1 \right] \right\} \quad 4$$

In Equation 4 the bulk modulus can be determined. The bulk modulus can be defined as the measure of a substance's resistance to uniform compression. As the compound in question has never been measured experimentally at high pressure, the best we can do is once again compare it to another cubic structure with a lithium metal,  $\text{Li}_3\text{OBr}$ . The bulk modulus of  $\text{Li}_3\text{OBr}$  has been seen experimentally to be 32 GPa [72], while in this calculated simulation  $\text{Li}_2(\text{OH})\text{Br}$  is found to be 49.6 GPa. This number seems reasonable and would most likely change as a larger sample structure was used giving higher accuracy.

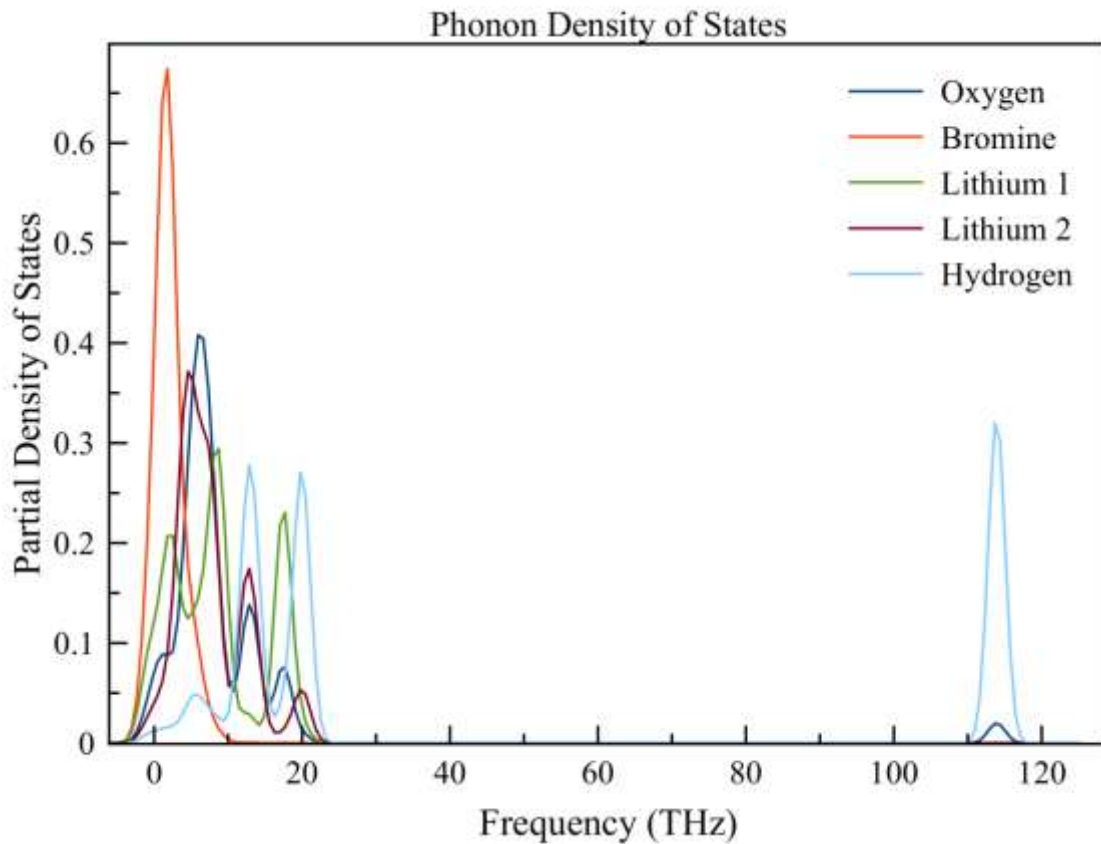


**Figure 24. Calculated phonon partial density of states of the 40-atom supercell model using the Phonopy code with a 2x2x2 k-point sampling**

In Figure 24 we present a partial phonon density of states plot. Different atomic contributions are delineated in the key. The software Phonopy® was used to calculate this particular density of states [73]. The K-point sampling was reduced to 2x2x2 for efficiency while still retaining accuracy.



# CHAPTER 5

## CONCLUSION

In this work, we created an accurate phase diagram of the high pressure calcium system using first-principles density functional theory calculations and *ab initio* evolutionary simulations to predict high pressure calcium structures. This led us to also finding the enthalpy of oxygen and corresponding structures that were accurate enough for our calculations in the formation of CaO and its various chemical compositions. Once the calcium and oxygen systems were found to be in good agreement with other experimental and theoretical work, we used the same DFT and USPEX methods in order to find the various structures of CaO and its various chemical compositions. Based on these findings, we then created a pressure/phase composition diagram for the Ca-O system. We then set out to determine whether or not the structures that had been found were either stable or meta-stable by determining the formation of enthalpies for each structure and comparing it to the naturally occurring CaO system by way of a stoichiometry plot. From our stoichiometry plot, we discovered that two compositions,  $\text{Ca}_2\text{O}_3$  and  $\text{CaO}_2$  are both stable at approximately 40 GPa.  $\text{Ca}_2\text{O}_3$  has the  $C2/c$  space group at 40 GPa and  $\text{CaO}_2$  has the  $Pnma$  space group both compounds remained stable at 90 GPa but transferred into the  $C2/m$  and  $P21c$  space groups respectively. When we began determining what happens at even higher pressures, we discovered that a third composition,  $\text{CaO}_3$  becomes stable at 150 GPa with the space group  $P-421$ .  $\text{Ca}_2\text{O}_3$  and  $\text{CaO}_2$  continue to remain stable at 150 GPa with space groups of  $I4/mmm$  and  $P21c$ . Visualizations were then made in order to see the crystal structures of each new stable structure. In order to get a better understanding of the properties of the new stable structures, we created density of states plots. We determined that all the new structures were in

fact insulators at all pressures, although a trend can be seen with the gap rapidly closing towards semi-conductors as pressures increase.

In our studies of the compound  $\text{Li}_2(\text{OH})\text{Br}$  we successfully modeled the structure within the limiting confines of the DFT program VASP. A supercell was used to create a successful model and was verified by comparing simulated XRD results against experimental XRD results. Once we successfully modeled the correct structure, we were then able to perform various structural analysis calculations to determine the properties of the compound. The electronic density of states was found and revealed information about the band gap, which turned out to be in good agreement with related experiments at a measurement of 4.0 eV. We were able to run simulations and gather results related to the pressure and volume behavior of the compound. From this information we then determined that the bulk modulus is 49.6 GPa, which is in good agreement with associated compounds. Finally the phonon density of states was completed which included the partial density of states from each corresponding atom.

## REFERENCES

1. S. Zhang, K. Xu, and T. Jow, *Electrochimica Acta* **49**, 1057 (2004).
2. R. Jeanloz, T. Ahrens, H. Mao, and P. Bell, *Science* **206**, 829 (1979).
3. Q. Zhu, A. Oganov, and A. Lyakhov, *ArXiv e-prints* **1211**, 6521 (2012).
4. W. Zhang, A. R. Oganov, A. F. Goncharov, Q. Zhu, S. E. Boulfelfel, A. O. Lyakhov, E. Stavrou, M. Somayazulu, V. B. Prakapenka, and Z. Konpkov, *Science* **342**, 1502 (2013).
5. Y. Ma, M. Eremets, A. R. Oganov, Y. Xie, I. Trojan, S. Medvedev, A. O. Lyakhov, M. Valle, and V. Prakapenka, *Nature* **458**, 182 (2009).
6. R. Szczes`niak and A. Durajski, *Solid State Commun.* **152**, 1018 (2012).
7. B. Li, Y. Ding, W. Yang, L. Wang, B. Zou, J. Shu, S. Sinogeikin, C. Park, G. Zou, and H.-k. Mao, *Proceedings of the National Academy of Sciences* **109**, 16459 (2012).
8. Y. Yao, J. S. Tse, Z. Song, D. D. Klug, J. Sun, and Y. Le Page, *Phys. Rev. B* **78**, 054506 (2008).
9. T. Ishikawa, H. Nagara, N. Suzuki, T. Tsuchiya, and J. Tsuchiya, *Phys. Rev. B* **81**, 092104 (2010).
10. H. Fujihisa, Y. Nakamoto, K. Shimizu, T. Yabuuchi, and Y. Gotoh, *Phys. Rev. Lett.* **101**, 095503 (2008).
11. Z. P. Yin, F. Gygi, and W. E. Pickett, *Phys. Rev. B* **80**, 184515 (2009).
12. Y. Nakamoto, M. Sakata, K. Shimizu, H. Fujihisa, T. Matsuoka, Y. Ohishi, and T. Kikegawa, *Phys. Rev. B* **81**, 140106 (2010).
13. T. Ishikawa, A. Ichikawa, H. Nagara, M. Geshi, K. Kusakabe, and N. Suzuki, *Phys. Rev. B* **77**, 020101 (2008).
14. A. M. Teweldeberhan and S. A. Bonev, *Phys. Rev. B* **78**, 140101 (2008).

15. J. Tse, S. Desgreniers, Y. Ohishi, and T. Matsuoka, *Scientific reports* **2**, (2012).
16. L. F. Lundegaard, G. Weck, M. I. McMahon, S. Desgreniers, and P. Loubeyre, *Nature (London)* **443**, 201 (2006).
17. H. Fujihisa, Y. Akahama, H. Kawamura, Y. Ohishi, O. Shimomura, H. Yamawaki, M. Sakashita, Y. Gotoh, S. Takeya, and K. Honda, *Phys. Rev. Lett.* **97**, 085503 (2006).
18. P. Hohenberg and W. Kohn, *Phys. Rev.* **136**, B864 (1964).
19. David Sholl and Janice Steckel, *Density Functional Theory: A Practical Introduction* (John Wiley & Sons, Inc., 2009).
20. J. P. Perdew and S. Kurth, Berlin, *Density Functionals for Non-relativistic Coulomb Systems in the New Century*. (Springer, 2003).
21. W. Kohn and L. J. Sham, *Phys. Rev.* **140**, A1133 (1965).
22. John P. Perdew and Yue Wang, *Phys. Rev. B* **45**, 13244 (1992).
23. J. P. Perdew and Alex Zunger, *Phys. Rev. B* **23**, 5048 (1981).
24. Weitao Parr, Robert G, Yang. *Density-Functional Theory of Atoms and Molecules* (Oxford: Oxford University Press, 1994).
25. D. M. Ceperly and B. J. Alder, *Phys. Rev. Lett.* **45**, 566 (1980).
26. J. P. Perdew, K. Burke, and M. Ernzerhof, *Phys. Rev. Lett.* **77**, 3865 (1996).
27. David C. Langreth and M. J. Mehl, *Phys. Rev. B* **28**, 1809 (1983).
28. John P. Perdew and Wang Yue, *Phys. Rev. B* **33**, 8800 (1986).
29. John P. Perdew, *Phys. Rev. Lett.* **55**, 1665 (1985).
30. John P. Perdew, *Phys. Rev. B* **33**, 8822, (1986).
31. John P. Perdew, Kieron Burke, and Matthias Ernzerhof *Phys. Rev. Lett.* **78**, 1396 (1997).
32. Georg Kresse and Jürgen Furthmüller. *Universität Wien, Sensengasse*, **8**, 1130 (2005).

33. G. Kresse and J. Hafner, Phys. Rev. B **47**, 558 (1993).
34. G. Kresse and D. Joubert, Phys. Rev. B **59**, 1758 (1999).
35. P. E. Blöchl, C. J. Först and J. Schimpl, Bull. Mater. Sci. **26**, 33 (2003)
36. P. E. Blöchl, Phys. Rev. B **50**, 17953 (1994).
37. E.R. Davidson, *Methods of Computational Physics*, **113** (Plenum, 1983).
38. B. Liu, Lawrence Berkeley Lab. Univ. of California, *Numerical Algorithms in Chemistry: Algebraic Methods*. (Berkeley Lab. Univ. of California, 1978).
39. D. M. Bylander, Leonard Kleinman, and Seongbok Lee, Phys. Rev. B **42** 1394 (1990).
40. S.A. Teukolsky W.H. Press, B.P. Flannery and W.T. Vetterling, *Numerical Recipes*. (Cambridge University Press, 2007).
41. S. Blügel. PhD Thesis. PhD thesis, RWTH Aachen, (1988).
42. D. D. Johnson, Phys. Rev. B **38**, 12807 (1988).
43. H. Akai and P.H. Dederichs, J. Phys. C **18**, (1985).
44. P. Pulay, Chem. Phys. Lett. **73**, 393 (1980).
45. S.A. Teukolsky, W.H. Press, B.P. Flannery and W.T. Vetterling, *Numerical Recipes*. (Cambridge University Press, 2007).
46. P. E. Blöchl, C. J. Först and J. Schimpl, Bull. Mater. Sci. **26**, 33 (2003).
47. H. J. Monkhorst and J. D. Pack, Phys. Rev. B **13**, 5188 (1976).
48. P. E. Blöchl, O. Jepsen, and O. K. Andersen, Phys. Rev. B **49**, 16223 (1994).
49. M. Methfessel and A. T. Paxton, Phys. Rev. B **40**, 3616 (1989).
50. P. E. Blochl, Phys. Rev. B **50**, 17953 (1994).
51. W. Kohn, A. D. Becke, and R. G. Parr, J. Phys. Chem. **100**, 12974 (1996).
52. A. R. Oganov and C. W. Glass, J. of Chem. Phys. **124**, 244704 (2006).

53. A. O. Lyakhov, A. R. Oganov, and M. Valle, *Comp. Phys. Comm.* **181**, 1623 (2010).
54. C. Glass, A. Oganov, and N. Hansen, *Comp. Phys. Comm.* **175**, 713 (2006).
55. A. O. Lyakhov, A. R. Oganov, H. T. Stokes, and Q. Zhu, *Comp. Phys. Comm.* **184**, 1172 (2013).
56. G. Kresse and J. Furthmuller, *Phys. Rev. B* **54**, 11169 (1996).
57. H. Olijnyk and W. Holzapfel, *Phys. Lett. A* **100**, 191 (1984).
58. A. R. Oganov and C. W. Glass, *J. Chem. Phys.* **124**, 244704 (2006).
59. L. F. Lundegaard, G. Weck, M. I. McMahon, S. Desgreniers, and P. Loubeyre, *Nature (London)* **434**, 201 (2006).
60. Desgreniers, S., Vohra, Y. K. and Ruoff, A. L. *J. Phys. Chem.* **94**, 1117 (1990).
61. K. Shimizu, K. Suhara, M. Ikumo, M. I. Eremets, and K. Amaya, *Nature* **393**, 767 (1998).
62. Y. Akahama, H. Kawamura, D. Hausermann, M. Hanfland, and O. Shimomura, *Phys. Rev. Lett.* **74**, 4690 (1995).
63. Y. M. Ma, A. R. Oganov & C. W. Glass, *Phys. Rev. B* **76**, 064101 (2007).
64. Y.A. Freiman, & H.J. Jodl, *Phys. Rep.* **401**, 1 (2004).
65. M. Sakata, Y. Nakamoto, K. Shimizu, T. Matsuoka, and Y. Ohishi, *Phys. Rev. B* **83**, 220512 (2011).
66. M. Mehl, R. Cohen, and H. Krakauer, *J. Geophys. Res.* **93**, 8009 (1988).
67. B. B. Karki and J. Crain, *J. Geophys Res* **103**, 12405 (1998).
68. K. Friese, A. Hönnerscheid, M. Jansen, *Z. für Kristallographie* **218**, 536 (2003).
69. C. F. Macrae, et al., *J. Appl. Cryst.* **41**, 466 (2008).
70. G. Kresse and J. Furthmüller, *Phys. Rev. B* **54**, 11169 (1996).
71. John Howard, PH. D. Dissertation, University of Nevada, Las Vegas, (2015).

72. W. Setyawan, R. M. Gaume, S. Lam, R. S. Feigelson, and S. Curtarolo, ACS  
Combinatorial Science **13**, 382 (2011).

73. <http://atztogo.github.io/phonopy/>

# CURRICULUM VITAE

## PROJECT EXPERIENCE:

### **Research at UNLV**

Jan 2012-Current

**Advisor:** Dr. Changfeng Chen

- Studied vacancy defects in carbon nanotubes under computer simulations.
- High pressure stable structure searches using evolutionary algorithms and density functional theory with various compounds.
- Work done using numerical parallel computation with over 100 processing cores.
- Data analysis of computational results from simulations.
- Numerical data analyzed and then visualized using various programs.

### **Research trip to Argonne National Laboratory**

2015

Accompanied Dr. Pravica and his research group in order learn about high pressure experimental physics procedures and how to implement them into my current work.

### **Research at UNLV**

Jan 2010-Dec 2011

**Advisor:** Dr. George Rhee

- Calculated rotational velocities of galaxies and their relation with dark matter.
- Data analysis done on files upwards of 5 gigabytes.
- Isolated specific information from real data taken by telescopes in orbit in order to make calculations.
- Data presentation presented using various software.

## INTERNSHIP:

### **National Securities Technologies Internship**

Summer 2012

- Operated and tested both hardware and software for radioactive detection equipment in conjunction with various radioactive sources.
- Tested several radio platforms to work with existing equipment and programs.
- Wrote the user manuals for various in house produced software.

## WORK EXPERIENCE

### **Graduate Assistant/Lab instructor**

2014-current

Responsible for assigning a letter grade and teaching labs of various undergraduate physics courses.

### **Tutoring**

2010-current

Tutoring UNLV students in science and math.

## COMPUTER SKILLS:

MATHEMATICA, S.M. PLOT, DS9, MS Office, VASP, P4VASP, USPEX, Sigma Plot, Vesta, Origin, Photoshop, editors such as emacs and VI, Linux, Mac and PC platforms.

## PROFESSIONAL ASSOCIATIONS

HiPSEC Member

2012-current



American Physics Society Student Member	2012-current
Argonne Advanced Photon Source User	2015-current
Society Of Physics Students	2010-current

**PUBLICATIONS**

Manuscript in preparation for submission “Ab Initio Structure Predictions for Calcium Oxide at High Pressures” 2016

**PRESENTATIONS**

**NNSA SSAP Symposium, Bethesda MD** 2016

Work on solid lithium based electrolytes was presented.

**NNSA SSAP Symposium, Santa Fe NM** 2015

Presented my work on computer simulations, evolutionary algorithms and structure changes within calcium oxide.

**HiPSEC annual meeting, Las Vegas NV** 2015

Poster presentation of my theoretical work with calcium oxide.

**HiPSEC annual review, Las Vegas NV** 2014

Presentation on theoretical work with sodium chloride and calcium oxide.

**HONORS AND AWARDS:**

Bob Davis Scholarship 2011-2013

UNLV Grant 2011-2013

NASA Space Grant Scholar 2011-2012

President of the Society of Physics Students 2010-2012

Gold medal at the Junior Olympics in Olympic weightlifting

**VOLUNTEER WORK:**

**Judge, Skybot challenge** 2015

A drone competition offered to local middle schools in order to further the education of STEM futures in students.

**Judge, regional high school and middle school Science Bowl** 2010-2016

A Science and math based trivia competition for middle and high school students used to further the interest in future STEM careers. Winners compete on a national level with finals taking place in Washington D.C.

**Li-ion/Hydrogen fuel cell car race competition** 2011-2014

An annual competition for middle school students to take part in. Li-ion battery technology and hydrogen fuel cells are the main topics focused on and used for the students cars.

**Volunteer, Lied animal shelter** 2010-2014

**Volunteer, U.M.C. hospital N.I.C.U. ward** 2010-2012